Structural and Multidisciplinary Optimization (2021) 64:3287–3309
https://doi.org/10.1007/s00158-021-02954-8

RESEARCH PAPER

Local stress constraints in topology optimization of structures subjected to arbitrary dynamic loads: a stress aggregation-free approach

Oliver Giraldo-Londoño[1] · Miguel A. Aguiló[2] · Glaucio H. Paulino[1]

Received: 28 October 2020 / Revised: 22 April 2021 / Accepted: 10 May 2021 / Published online: 15 September 2021

Abstract

We present an augmented Lagrangian-based approach for stress-constrained topology optimization of structures subjected to general dynamic loading. The approach renders structures that satisfy the stress constraints locally at every time step. To solve problems with a large number of stress constraints, we normalize the penalty term of the augmented Lagrangian function with respect to the total number of constraints (i.e., the number of elements in the mesh times the number of time steps). Moreover, we solve the stress-constrained problem effectively by penalizing constraints associated with high stress values more severely than those associated with low stress values. We integrate the equations of motion using the HHT-α method and conduct the sensitivity analysis consistently with this method via the "discretize-then-differentiate" approach. We present several numerical examples that elucidate the effectiveness of the approach to solve dynamic, stress-constrained problems under several loading scenarios including loads that change in magnitude and/or direction and loads that change in position as a function of time.

Keywords Local stress constraints · Topology optimization · Augmented Lagrangian · HHT-α method · Newmark-β method · Elastodynamics

1 Introduction

When considering material failure, a dynamic topology optimization formulation should include local stress constraints at each time step of the dynamic analysis, so that the material strength is not exceeded at any point of the structure for the duration of the dynamic event. Although consistent with the local definition of stress, a formulation of this type requires a tremendous amount of stress constraints that need to be handled by the optimizer, which adds complexity to the already challenging static, stress-constrained problem. In fact, one could argue that the large number of stress constraints together with other well-known challenges related to the stress-constrained problem (i.e., stress constraint nonlinearity and degeneracy of the solution space) may be the reason why a stress-constrained topology formulation for structures subjected to general dynamic loading has not been introduced thus far. In this study, we introduce topology optimization of structures subjected to general dynamic loading, in the time domain, while considering local stress constraints at every time step.

The literature on dynamic topology optimization is vast, yet the majority of studies focus on stiffness maximization methods or other dynamic performance measures, while neglecting the effects of material strength. In an effort to account for the effect of dynamic loads in design, two main directions have been pursued for topology optimization of elastodynamic problems under forced vibration: frequency-domain methods and time-domain methods. Frequency-domain methods are less computationally expensive than time-domain methods because the latter require a time integration scheme to solve the dynamic analysis problem. Frequency-domain approaches are useful for periodic loading or when modal quantities are of interest (e.g.,

Responsible Editor: Gengdong Cheng

✉ Glaucio H. Paulino
paulino@gatech.edu

[1] School of Civil and Environmental Engineering, Georgia Institute of Technology, 790 Atlantic Drive, Atlanta, GA 30332, USA

[2] Simulation and Modeling Sciences, Sandia National Laboratories, P.O. Box 5800, Albuquerque, NM 87185, USA

eigenfrequency optimization problems). Using frequency-domain techniques, a study that has considered stress constraints in dynamic topology optimization is that by Long et al. (2019). However, our main goal is to consider stress constraints in the time domain. The formulation introduced herein could be used, for example, to design structures subjected to shock/impact loading. These types of structures or structural components are, in general, subjected to non-periodic dynamic loading, and thus, their design requires time-domain analysis.

Dynamic topology optimization in the time domain has been used in several applications. For example, Min et al. (1999) used it to minimize the mean dynamic compliance, Turteltaub (2005) to minimize the time-averaged stress energy of functionally graded composites, Dahl et al. (2008) to generate band-gap structures, Le et al. (2012) to tailor energy propagation through microstructures, Zhang and Kang (2014) to reduce the transient response of piezoelectric structures, and Zhao and Wang (2017) to minimize either displacements at a target node or to minimize the dynamic compliance. In those studies, the dynamic problem is solved using traditional time integration schemes (e.g., the Newmark-β method). To solve the dynamic problem in an approximate way, other researchers have adopted model reduction techniques, which use different modal superposition methods (e.g., Yoon 2010; Zhao and Wang 2016). Dynamic topology optimization in the time domain has been used for applications beyond those discussed here, yet for the sake of brevity, the interested reader is referred to Giraldo-Londoño and Paulino (2021a) and the references therein for a more comprehensive literature review on the topic. Among the studies discussed here, none has considered stress constraints in the time domain.

In this work, we introduce a framework for topology optimization of structures subjected to general dynamic loading, which considers stress constraints locally for each time step of the dynamic analysis. To solve the dynamic, stress-constrained problem, we adopt an augmented Lagrangian (AL) formulation, building upon our previous work on static, stress-constrained topology optimization (Senhora et al. 2020; Giraldo-Londoño and Paulino 2020, 2021b). In our previous work, we employ the AL method in its traditional form (Nocedal and Wright 2006; Bertsekas 1999), yet we normalize the penalization term of the AL function (i.e., all terms containing the stress constraints) with respect to the number of constraints, which allows the method to solve problems with a large number of constraints. As shown by Senhora et al. (2020), the normalization scheme leads to the solution of problems with a number of stress constraints ranging from a few thousands to over a million or beyond. Because the dynamic, stress-constrained problem is more challenging than the static one, we apply suitable modifications to the AL formulation, which enable us to solve the new problem effectively.

To solve the dynamic, stress-constrained problem efficiently, we use a gradient-based optimization algorithm for which we require the sensitivity of the AL function. We compute the sensitivity using the adjoint variable method based on the *discretize-then-differentiate* approach (Jensen et al. 2014), so that the adjoint problem is constructed in terms of state and time variables that have both been discretized a priori. Because the discretize-then-differentiate approach is tied to a particular time integration scheme, we adopt the HHT-α method (Hilber et al. 1977) to solve the dynamic analysis problem. The HHT-α method is a generalization of the Newmark-β method (Newmark 1959) and reduces to the Newmark-β method for $\alpha = 0$. The HHT-α method is general enough and reduces to other classical time integration schemes given a proper choice of parameters.

The remainder of this paper is organized as follows. Section 2 discusses the topology optimization statement for dynamic, stress-constrained topology optimization, and Section 3 discusses the HHT-α method used to solve the dynamic analysis problem. We discuss the AL-based formulation for dynamic, stress-constrained topology optimization in Section 4, and present the *discretize-then-differentiate* adjoint sensitivity analysis in Section 5. Moreover, Section 6 contains some implementation details, and Section 7 discusses the results of four numerical examples, which we solve to show the effectiveness of the approach. We finalize the paper with some concluding remarks in Section 8. Afterwards, we provide three appendices, where the first shows details of the design variable update scheme, the second shows convergence plots for some of the numerical examples, and the third shows the nomenclature used in this study.

2 Stress-constrained formulation for elastodynamics

We aim to solve mass minimization topology optimization problems with local stress constraints imposed at all time steps. In a discretized setting, our objective is to minimize the volume fraction, $f(\mathbf{z})$, of a structure subjected to dynamic loading, such that the stresses are limited via local stress constraints, $g_{\ell i}(\mathbf{z}, \mathbf{u}_i) \leq 0$ for all time steps $i = 0, \ldots, N_t$ and at all stress evaluation points $\ell = 1, \ldots, N$ (e.g., defined at the centroid of each finite element). The topology is defined by the design variables, $\mathbf{z} \in [0, 1]^N$, while the physical response of the system (i.e., the displacement field) is given by the state variables, $\mathbf{u}_i, \quad i = 0, \ldots, N_t$, which we obtain from the solution of the discretized equations of

motion of a continuum system. Mathematically, we state the problem as follows:[1]

$$\begin{aligned} \min_{\mathbf{z}\in[0,1]^N} \quad & f(\mathbf{z}) = \frac{\mathbf{A}^T m_V(\mathbf{y})}{\mathbf{A}^T\mathbf{1}} \\ \text{s.t.} \quad & g_{\ell i}(\mathbf{z},\mathbf{u}_i) \le 0, \quad i=0,\ldots,N_t, \quad \ell=1,\ldots,N \\ \text{with:} \quad & \mathbf{M}\ddot{\mathbf{u}}_i + \mathbf{C}\dot{\mathbf{u}}_i + \mathbf{K}\mathbf{u}_i = \mathbf{f}_i, \quad i=0,\ldots,N_t, \end{aligned} \tag{1}$$

where $\mathbf{A} = \{|\Omega_\ell|\}_{\ell=1}^N$ is the vector of element areas (2D) or volumes (3D),

$$m_V(y_\ell) = \frac{\tanh(\bar{\beta}\bar{\eta}) + \tanh(\bar{\beta}(y_\ell - \bar{\eta}))}{\tanh(\bar{\beta}\bar{\eta}) + \tanh(\bar{\beta}(1-\bar{\eta}))}, \tag{2}$$

is a volume interpolation function, defined by the threshold projection function (Wang et al. 2011), which we use to compute the element volume fractions as a function of the filtered densities. Parameter $\bar{\beta}$ controls the aggressiveness of the threshold projection and parameter $\bar{\eta}$ is the threshold projection density. The vector $\mathbf{y} = \{y_\ell\}_{\ell=1}^N$ contains the filtered densities for all elements, and it is obtained as $\mathbf{y} = \mathbf{P}\mathbf{z}$, where $\mathbf{P}$ is the filter matrix, which we compute as (Zegard and Paulino 2016):

$$P_{ij} = \frac{w_{ij}A_j}{\sum_{k=1}^N w_{ik}A_k}, \quad \text{with} \quad w_{ij} = \max\left(0, 1 - \frac{\|\mathbf{x}_i - \mathbf{x}_j\|_2}{R}\right)^q, \tag{3}$$

where A_j is the volume (3D) or area (2D) of the j-th finite element, $\|\mathbf{x}_i - \mathbf{x}_j\|_2$ is the Eucledian distance between the centroids of elements i and j, respectively, q is the filter exponent, and R is the filter radius. Finally, $\mathbf{M}\ddot{\mathbf{u}}_i + \mathbf{C}\dot{\mathbf{u}}_i + \mathbf{K}\mathbf{u}_i = \mathbf{f}_i$ is the discretized equation of motion for elastodynamics,[2] which we solve to obtain the time-dependent displacement field necessary to evaluate the stress constraints at each time step, i.

2.1 Mass, stiffness, and damping matrices

To solve the equation of motion, $\mathbf{M}\ddot{\mathbf{u}}_i + \mathbf{C}\dot{\mathbf{u}}_i + \mathbf{K}\mathbf{u}_i = \mathbf{f}_i$, we need to obtain the mass, stiffness, and damping matrices at each optimization step. The mass and stiffness matrices are obtained as

$$\mathbf{M} = \sum_{\ell=1}^N \widetilde{m}_V(y_\ell)\mathbf{m}_\ell \quad \text{and} \quad \mathbf{K} = \sum_{\ell=1}^N \widetilde{m}_E(y_\ell)\mathbf{k}_\ell, \tag{4}$$

where $\sum_{\ell=1}^N$ is the finite element (FE) assembly operator, and

$$\mathbf{m}_\ell = \int_{\Omega_\ell} \rho_0 \mathbf{N}_\ell^T \mathbf{N}_\ell \mathrm{d}\mathbf{x} \quad \text{and} \quad \mathbf{k}_\ell = \int_{\Omega_\ell} \mathbf{B}_\ell^T \mathbf{D}_0 \mathbf{B}_\ell \mathrm{d}\mathbf{x} \tag{5}$$

are the mass and stiffness matrices of element ℓ, respectively, in which ρ_0 and $\mathbf{D}_0$ are the mass density and the material moduli matrix of the solid material, respectively; $\mathbf{N}_\ell$ is the matrix of shape functions; and $\mathbf{B}_\ell$ is the strain-displacement matrix. Function

$$\widetilde{m}_V(y_\ell) = \epsilon + (1-\epsilon)m_V(y_\ell)$$

is the volume interpolation function modified by an Ersatz parameter, $\epsilon \ll 1$, and function

$$\widetilde{m}_E(y_\ell) = \epsilon + (1-\epsilon)m_E(y_\ell)$$

is a stiffness interpolation function, which we evaluate in terms of the RAMP function (Stolpe and Svanberg 2001; Bendsøe and Sigmund 2003) as follows:

$$m_E(y_\ell) = \frac{m_V(y_\ell)}{1 + p_0[1 - m_V(y_\ell)]}, \tag{6}$$

where p_0 is the RAMP penalization parameter. The Ersatz parameter is used to prevent numerical instabilities arising when $y_\ell \to 0$.

To account for energy losses, we consider proportional damping (for the sake of simplicity and in the absence of additional information) such that the damping matrix, $\mathbf{C}$, is obtained as a linear combination of the mass and the stiffness matrices, as follows:

$$\mathbf{C} = \alpha_r \mathbf{M} + \beta_r \mathbf{K}, \tag{7}$$

where α_r and β_r are the Rayleigh damping coefficients.

2.2 Stress constraint definition

The stress constraints $g_{\ell i}$ in (1) are based on the *polynomial vanishing constraint* introduced by Giraldo-Londoño and Paulino (2020). Specifically, the stress constraints are evaluated as

$$\begin{aligned} g_{\ell i}(\mathbf{z},\mathbf{u}_i) &= \widetilde{m}_E(y_\ell)\Lambda_{\ell i}(\Lambda_{\ell i}^2 + 1) \le 0, \\ & \qquad i=0,\ldots,N_t, \quad \ell=1,\ldots,N, \end{aligned} \tag{8}$$

where

$$\Lambda_{\ell i} = \sigma_{\ell i}^v/\sigma_{\lim} - 1 \tag{9}$$

[1] Conceptually, the equation, $\mathbf{M}\ddot{\mathbf{u}}_i + \mathbf{C}\dot{\mathbf{u}}_i + \mathbf{K}\mathbf{u}_i = \mathbf{f}_i$, in (1) is the discrete counterpart of the equation of motion, $\mathbf{M}\ddot{\mathbf{u}} + \mathbf{C}\dot{\mathbf{u}} + \mathbf{K}\mathbf{u} = \mathbf{f}$. However, the actual equation of motion used in the numerical implementation is given in (12).

[2] In the current formulation, we solve the equation of motion via the HHT-α method, as we discuss in detail later.

is a failure function based on the von Mises strength criterion,[3] where

$$\sigma_{\ell i}^{v} = \sqrt{\boldsymbol{\sigma}_{\ell i}^{T} \mathbf{V}_0 \boldsymbol{\sigma}_{\ell i}} \tag{10}$$

is the von Mises stress at the centroid of element ℓ and at time step i; $\boldsymbol{\sigma}_{\ell i} = [\sigma_{11}^{\ell i}, \sigma_{22}^{\ell i}, \sigma_{12}^{\ell i}]^T$ is the vector of Cauchy stresses (in Voigt notation) evaluated at the centroid of element ℓ and at time step i;

$$\mathbf{V}_0 = \begin{bmatrix} 1 & -1/2 & 0 \\ -1/2 & 1 & 0 \\ 0 & 0 & 3 \end{bmatrix}$$

is a matrix of constant coefficients; and σ_{lim} is the material stress limit in uniaxial tension. The vector of Cauchy stresses at time step i is computed as

$$\boldsymbol{\sigma}_{\ell i} = \mathbf{D}_0 \mathbf{B}_\ell \mathbf{u}_{\ell i}, \tag{11}$$

where $\mathbf{u}_{\ell i}$ is the displacement vector of element ℓ at time step i.

The von Mises stresses given in (10) are computed using the elastic properties of solid material (because $\boldsymbol{\sigma}_{\ell i}$ are computed using $\mathbf{D}_0$) rather than using elastic properties that have been interpolated for intermediate density values. Given that the von Mises stresses are computed using properties of the solid material and the stress constraints, $g_{\ell i}(\mathbf{z}, \mathbf{u}_i)$, in (1) are a variation of the traditional vanishing constraints (Cheng and Jiang 1992), the solution space associated with the optimization statement (1) is unrelaxed. This is unlike typical approaches based, e.g., on the ε-relaxation approach (Cheng and Guo 1997) or the qp-relaxation approach (Bruggi 2008), in which the feasible solution space is relaxed.

3 The HHT-α method

Similarly to Giraldo-Londoño and Paulino (2021a), this study solves the dynamic analysis problem via the HHT-α method (Hilber et al. 1977). This method is a generalization of the classical Newmark-β (Newmark 1959), and reduces to the Newmark method for $\alpha = 0$. The HHT-α method contains numerical damping controlled by a parameter, α, which helps attenuate the response controlled by high-frequency modes, while leaving that controlled by low-frequency modes essentially unaffected. The HHT-α method uses the parameter α to modify the equation of motion (EOM) by introducing a numerical lag to damping forces, restoring forces, and external forces, as follows:

$$\begin{aligned} \mathbf{M}\ddot{\mathbf{u}}_i &+ (1-\alpha)\mathbf{C}\dot{\mathbf{u}}_i + \alpha\mathbf{C}\dot{\mathbf{u}}_{i-1} + (1-\alpha)\mathbf{K}\mathbf{u}_i + \alpha\mathbf{K}\mathbf{u}_{i-1} \\ &= (1-\alpha)\mathbf{f}_i + \alpha\mathbf{f}_{i-1}, \quad i = 1, \ldots, N_t. \end{aligned} \tag{12}$$

The modified EOM is solved together with the Newmark-β finite difference (FD) relationships,

$$\begin{aligned} \mathbf{u}_i &= \mathbf{u}_{i-1} + \Delta t \dot{\mathbf{u}}_{i-1} + \Delta t^2 \left[\left(\frac{1}{2} - \beta \right) \ddot{\mathbf{u}}_{i-1} + \beta \ddot{\mathbf{u}}_i \right] \\ \dot{\mathbf{u}}_i &= \dot{\mathbf{u}}_{i-1} + \Delta t \left[(1-\gamma)\ddot{\mathbf{u}}_{i-1} + \gamma \ddot{\mathbf{u}}_i \right]. \end{aligned} \tag{13}$$

We replace relationships (13) into the modified EOM (12) and rewrite it in residual form, as follows:

$$\mathbf{R}_i = \mathbf{M}_1 \ddot{\mathbf{u}}_i + \mathbf{M}_0 \ddot{\mathbf{u}}_{i-1} + \mathbf{C}_0 \dot{\mathbf{u}}_{i-1} + \mathbf{K}\mathbf{u}_{i-1} - (1-\alpha)\mathbf{f}_i - \alpha\mathbf{f}_{i-1} = \mathbf{0}, \tag{14}$$

where

$$\begin{aligned} \mathbf{M}_1 &= \mathbf{M} + (1-\alpha)\gamma\Delta t\mathbf{C} + (1-\alpha)\beta\Delta t^2\mathbf{K}, \\ \mathbf{M}_0 &= (1-\alpha)(1-\gamma)\Delta t\mathbf{C} + (1-\alpha)\left(\frac{1}{2} - \beta\right)\Delta t^2\mathbf{K}, \quad \text{and} \\ \mathbf{C}_0 &= \mathbf{C} + (1-\alpha)\Delta t\mathbf{K}. \end{aligned} \tag{15}$$

To solve the dynamic analysis problem, first we solve (14) for $\ddot{\mathbf{u}}_i$ and use it to update $\mathbf{u}_i$ and $\dot{\mathbf{u}}_i$ using (13). For $i = 0$, we use the initial conditions, $\mathbf{u}_0$ and $\dot{\mathbf{u}}_0$ and compute the initial acceleration vector as $\ddot{\mathbf{u}}_0 = \mathbf{M}^{-1}(\mathbf{f}_0 - \mathbf{C}\dot{\mathbf{u}}_0 - \mathbf{K}\mathbf{u}_0)$.

4 AL-based method tailored to elastodynamics

To solve the dynamic, stress-constrained problem, we adopt a slightly modified version of the AL-based approach by Giraldo-Londoño and Paulino (2020, 2021b), in which the penalty term of the AL function is normalized with respect to the number of constraints. For the static, stress-constrained problem, the number of constraints (for a single load case) is chosen as the number of elements, N (different choices are possible). However, given that the dynamic, stress-constrained problem imposes one constraint per element and per time step, we need to modify the term used to normalize the penalty of the AL function. For the dynamic, stress-constrained problem, we normalize the penalty term of the AL function using the factor, NN_t, so

[3] Although different strength criteria including von Mises, Tresca, Drucker-Prager, and Mohr–Coulomb can be considered by means of the unified strength function by Giraldo-Londoño and Paulino (2020), here we only consider the von Mises strength criterion (von Mises 1913) to keep the focus of the study on the dynamic problem.

that we solve the following optimization problem at each step, k, of the AL method:[4]

$$\min_{\mathbf{z}\in[0,1]^N} J^{(k)}(\mathbf{z}, \mathbf{u}_0, \ldots, \mathbf{u}_{N_t}) = f(\mathbf{z}) + \frac{1}{NN_t}\sum_{i=0}^{N_t}\sum_{\ell=1}^{N}\left[\lambda_{\ell i}^{(k)} h_{\ell i}(\mathbf{z}, \mathbf{u}_i) + \frac{\mu_{\ell i}^{(k)}}{2} h_{\ell i}(\mathbf{z}, \mathbf{u}_i)^2\right], \tag{16}$$

where

$$h_{\ell i}(\mathbf{z}, \mathbf{u}_i) = \max\left(g_{\ell i}(\mathbf{z}, \mathbf{u}_i), -\frac{\lambda_{\ell i}^{(k)}}{\mu_{\ell i}^{(k)}}\right), \tag{17}$$

$$\lambda_{\ell i}^{(k+1)} = \lambda_{\ell i}^{(k)} + \mu_{\ell i}^{(k)} h_{\ell i}(\mathbf{z}^{(k)}, \mathbf{u}_i), \text{ and} \tag{18}$$

$$\mu_{\ell i}^{(k+1)} = \min\left(\alpha_{\ell i}\mu_{\ell i}^{(k)}, \mu_{\max}\right). \tag{19}$$

Parameters $\lambda_{\ell i}^{(k)}$ are Lagrange multiplier estimators at the k-th step of the augmented Lagrangian method and are updated as shown in (18) (Nocedal and Wright 2006). Moreover, parameters $\mu_{\ell i}^{(k)}$ are the quadratic penalty terms, which we update as shown in (19). The initial values, $\lambda_{\ell i}^{(1)}$ and $\mu_{\ell i}^{(1)}$, are selected by the user.[5]

As shown in (19), we update the quadratic penalty terms using parameters $\alpha_{\ell i} > 1$ and impose an upper limit, $\mu_{\max}$, to avoid ill-conditioning. We introduce the following expression to compute the update parameters:

$$\alpha_{\ell i} = 2\tilde{\alpha}\left(\frac{\widetilde{\sigma}_{\ell i}^{v} + 1}{\widetilde{\sigma}_{\ell i}^{v} + 2}\right), \tag{20}$$

where $\tilde{\alpha} > 1$ is a constant term and

$$\widetilde{\sigma}_{\ell i}^{v} = \widetilde{m}_E(y_\ell)\sigma_{\ell i}^{v}/\sigma_{\text{lim}} \tag{21}$$

is the relaxed von Mises stress of element ℓ at time step i. We define the expression to compute $\alpha_{\ell i}$ such that $\alpha_{\ell i} \to \tilde{\alpha}$ when $\widetilde{\sigma}_{\ell i}^{v} \to 0$, and $\alpha_{\ell i} \to 2\tilde{\alpha}$ when $\widetilde{\sigma}_{\ell i}^{v} \to \infty$, which is intended to penalize constraints associated with high stress values more severely than those associated with low stress values. The relaxed von Mises stresses given in (21) are used to update the quadratic penalty terms in (19) and to plot the von Mises stress maps in Section 7. However, these relaxed stresses are not used to evaluate the stress constraints. Instead, the stress constraints are evaluated based on the apparent local von Mises stresses computed using the elastic parameters of the solid material, as shown in (10)–(11), which we employ to preserve the shape of the feasible solution space.

We highlight two main differences between the AL function in (16) and that used by Giraldo-Londoño and Paulino (2020, 2021b). First, the new AL function uses a different normalization term (i.e., NN_t) to account for the increasing number of constraints. Second, the new function considers one quadratic penalty term, $\mu_{\ell i}^{(k)}$, for each constraint, in contrast to the single quadratic penalty term, $\mu^{(k)}$, used by Giraldo-Londoño and Paulino (2020, 2021b). We found that these changes are necessary to improve the robustness of the approach to solve the dynamic topology optimization problem. The use of one quadratic penalty term per constraint is particularly important because it allows penalizing constraints independently, which is useful for time steps in which the stress limit is not exceeded in any element. Next we provide a couple of remarks.

Remark 1 The literature on stress-constrained topology optimization typically handles the stress constraints using aggregation techniques, so that the local constraints are aggregated into one global or a few regional constraints (e.g., see Le et al. 2010; Lee et al. 2012; Luo et al. 2013; De Leon et al. 2015; Holmberg et al. 2013a; Xia et al. 2018). These clustering techniques aim to approximate the maximum stress in the design domain using a smooth approximation of the maximum function, such as the p-norm function (Park 1995) or the KS function (Kreisselmeier and Steinhauser 1979). The quality of the approximation using either of these functions depends on the parameters that define them (e.g., they depend on the value of p if the p-norm function is used). Thus, the quality of the solutions obtained using these aggregation approaches will depend on the parameters of the approximation. More importantly, the solution to which one arrives when using aggregation approaches is not the same as the solution of the original optimization problem with local stress constraints (the two problem statements are different).

Remark 2 The AL method is fundamentally different from stress aggregation approaches because it does not require the use of a surrogate inequality based on a smooth approximation of the maximum function. Instead, the AL method solves the original optimization problem with local constraints as a sequence of minimization problems, i.e., the AL sub-problems (16), whose solution is expected

[4] Note that $h_{\ell i}(\mathbf{z}, \mathbf{u}_i)^2$ means $[h_{\ell i}(\mathbf{z}, \mathbf{u}_i)]^2$.

[5] The values of $\lambda_{\ell i}^{(1)}$, $\mu_{\ell i}^{(1)}$, and $\mu_{\max}$ need to be found via an initial calibration process. We have noticed that $\lambda_{\ell i}^{(1)} = 0$ is a suitable choice, and thus, the calibration process is typically conducted to find $\mu_{\ell i}^{(1)}$ and $\mu_{\max}$. As a general guideline, $\mu_{\ell i}^{(1)}$ should not be too small because it slows down convergence and $\mu_{\max}$ should not be too large because it leads to numerical instability. Once appropriate values for $\mu_{\ell i}^{(1)}$ and $\mu_{\max}$ have been found, our experience indicates that they can be used to solve different problems independently of the domain geometry, mesh size, and number of time steps.

to converge to that of the original optimization problem with local constraints. Moreover, it has been found that the AL method exhibits global convergence properties even for problems with degenerated constraints (Izmailov et al. 2012; Andreani et al. 2012). Such global convergence attributes cannot be guaranteed by stress aggregation approaches.

5 Discretize-then-differentiate: adjoint sensitivity analysis

Sensitivity analysis is a fundamental part of any topology optimization formulation solved using gradient-based algorithms. Given that topology optimization problems usually involve thousands or even millions of design variables, it is of the utmost importance that the sensitivity analysis is conducted efficiently. In an effort to reduce the computational cost, we adopt the adjoint method for sensitivity analysis. Employing the adjoint method, sensitivity analysis in dynamic topology optimization has traditionally been conducted using either of two main approaches. The first, which is known as the *differentiate-then-discretize* approach, uses discretized state variables and considers time as a continuous variable, leading to an adjoint system in the form of a terminal boundary value problem, which is then discretized in time and solved using a time integration technique similar to that used to solve the primal problem. The *differentiate-then-discretize* approach is the most widely used in dynamic topology optimization (e.g., refer to Arora and Cardoso 1992; Turteltaub 2005; Nomura et al. 2007; Dahl et al. 2008; Elesin et al. 2012; Mello et al. 2012; Zhang and Kang 2014; Zhao and Wang 2016, 2017).

The second, known as the *discretize-then-differentiate* approach, applies the adjoint method to the discretized problem (both in space and time), so it is tied to a specific time integration scheme. Consequently, the discretize-then-differentiate approach tends to be more cumbersome than the differentiate-then discretize approach. However, Jensen et al. (2014) demonstrated that the differentiate-then-discretize approach leads to consistency errors (i.e., differences between the computed sensitivities and the exact sensitivities of the numerical model), which may cause problems for large time steps. In pursuit of a consistent sensitivity analysis, the present work adopts the discretize-then-differentiate approach (Le et al. 2012; Jensen et al. 2014; Nakshatrala and Tortorelli 2016) consistently with the HHT-α method discussed previously. Because the HHT-α method is general, it can be simplified to other classical numerical integration schemes (e.g., trapezoidal, explicit central differences, average constant acceleration), and thus, the sensitivities derived here can work for other classical methods.

Using the discretize-then-differentiate approach, we obtain the sensitivity of the AL function as

$$\frac{\mathrm{d}J^{(k)}}{\mathrm{d}z_e} = \frac{\partial J^{(k)}}{\partial z_e} + \sum_{i=1}^{N_t} \frac{\partial J^{(k)}}{\partial \mathbf{u}_i} \cdot \frac{\partial \mathbf{u}_i}{\partial z_e}. \tag{22}$$

To eliminate the terms $\partial \mathbf{u}_i / \partial z_e$ from the expression above, we use the residual term (14) together with the initial condition

$$\mathbf{R}_0 = \mathbf{M}\ddot{\mathbf{u}}_0 + \mathbf{C}\dot{\mathbf{u}}_0 + \mathbf{K}\mathbf{u}_0 - \mathbf{f}_0 = \mathbf{0} \tag{23}$$

and the Newmark-β FD relationships (13), which we rewrite in residual form as follows:

$$\begin{aligned}
\mathbf{P}_i &= -\mathbf{u}_i + \mathbf{u}_{i-1} + \Delta t \dot{\mathbf{u}}_{i-1} + \Delta t^2 \left[\left(\frac{1}{2} - \beta \right) \ddot{\mathbf{u}}_{i-1} + \beta \ddot{\mathbf{u}}_i \right] \\
&= \mathbf{0}, \quad i = 1, \ldots, N_t \\
\mathbf{Q}_i &= -\dot{\mathbf{u}}_i + \dot{\mathbf{u}}_{i-1} + \Delta t \left[(1-\gamma) \ddot{\mathbf{u}}_{i-1} + \gamma \ddot{\mathbf{u}}_i \right] \\
&= \mathbf{0}, \quad i = 1, \ldots, N_t.
\end{aligned} \tag{24}$$

We introduce adjoint variables, $\boldsymbol{\xi}_i$, $\boldsymbol{\mu}_i$, and $\boldsymbol{\nu}_i$ for $i = 0, \ldots N_t$, resembling *pseudo-displacement*, *pseudo-velocity*, and *pseudo-acceleration* fields, respectively, and rewrite (22) as

$$\begin{aligned}
\frac{\mathrm{d}J^{(k)}}{\mathrm{d}z_e} &= \frac{\partial J^{(k)}}{\partial z_e} + \sum_{i=0}^{N_t} \frac{\partial J^{(k)}}{\partial \mathbf{u}_i} \cdot \frac{\partial \mathbf{u}_i}{\partial z_e} \\
&\quad + \sum_{i=0}^{N_t} \boldsymbol{\xi}_i^T \left[\frac{\partial \mathbf{R}_i}{\partial z_e} + \sum_{\ell=0}^{N_t} \left(\frac{\partial \mathbf{R}_i}{\partial \mathbf{u}_\ell} \cdot \frac{\partial \mathbf{u}_\ell}{\partial z_e} + \frac{\partial \mathbf{R}_i}{\partial \dot{\mathbf{u}}_\ell} \cdot \frac{\partial \dot{\mathbf{u}}_\ell}{\partial z_e} + \frac{\partial \mathbf{R}_i}{\partial \ddot{\mathbf{u}}_\ell} \cdot \frac{\partial \ddot{\mathbf{u}}_\ell}{\partial z_e} \right) \right] \\
&\quad + \sum_{i=1}^{N_t} \boldsymbol{\mu}_i^T \left[\frac{\partial \mathbf{P}_i}{\partial z_e} + \sum_{\ell=0}^{N_t} \left(\frac{\partial \mathbf{P}_i}{\partial \mathbf{u}_\ell} \cdot \frac{\partial \mathbf{u}_\ell}{\partial z_e} + \frac{\partial \mathbf{P}_i}{\partial \dot{\mathbf{u}}_\ell} \cdot \frac{\partial \dot{\mathbf{u}}_\ell}{\partial z_e} + \frac{\partial \mathbf{P}_i}{\partial \ddot{\mathbf{u}}_\ell} \cdot \frac{\partial \ddot{\mathbf{u}}_\ell}{\partial z_e} \right) \right] \\
&\quad + \sum_{i=1}^{N_t} \boldsymbol{\nu}_i^T \left[\frac{\partial \mathbf{Q}_i}{\partial z_e} + \sum_{\ell=0}^{N_t} \left(\frac{\partial \mathbf{Q}_i}{\partial \mathbf{u}_\ell} \cdot \frac{\partial \mathbf{u}_\ell}{\partial z_e} + \frac{\partial \mathbf{Q}_i}{\partial \dot{\mathbf{u}}_\ell} \cdot \frac{\partial \dot{\mathbf{u}}_\ell}{\partial z_e} + \frac{\partial \mathbf{Q}_i}{\partial \ddot{\mathbf{u}}_\ell} \cdot \frac{\partial \ddot{\mathbf{u}}_\ell}{\partial z_e} \right) \right].
\end{aligned} \tag{25}$$

The terms $\mathbf{P}_i$ and $\mathbf{Q}_i$ have no explicit dependence on the design variables, so $\frac{\partial \mathbf{P}_i}{\partial z_e} = \mathbf{0}$ and $\frac{\partial \mathbf{Q}_i}{\partial z_e} = \mathbf{0}$. Moreover, since the initial conditions are independent of the design variables, we also have that $\frac{\partial \mathbf{u}_0}{\partial z_e} = \mathbf{0}$ and $\frac{\partial \dot{\mathbf{u}}_0}{\partial z_e} = \mathbf{0}$. These simplifications allow us rewrite (25) more conveniently as

$$\begin{aligned}
\frac{\mathrm{d}J^{(k)}}{\mathrm{d}z_e} &= \frac{\partial J^{(k)}}{\partial z_e} + \sum_{i=0}^{N_t} \boldsymbol{\xi}_i^T \frac{\partial \mathbf{R}_i}{\partial z_e} \\
&\quad + \left(\boldsymbol{\xi}_0^T \frac{\partial \mathbf{R}_0}{\partial \ddot{\mathbf{u}}_0} + \boldsymbol{\xi}_1^T \frac{\partial \mathbf{R}_1}{\partial \ddot{\mathbf{u}}_0} + \boldsymbol{\mu}_1^T \frac{\partial \mathbf{P}_1}{\partial \ddot{\mathbf{u}}_0} + \boldsymbol{\nu}_1^T \frac{\partial \mathbf{Q}_1}{\partial \ddot{\mathbf{u}}_0} \right) \cdot \frac{\partial \ddot{\mathbf{u}}_0}{\partial z_e} \\
&\quad + \sum_{i=1}^{N_t} \sum_{\ell=1}^{N_t} \left(\boldsymbol{\xi}_\ell^T \frac{\partial \mathbf{R}_\ell}{\partial \mathbf{u}_i} + \boldsymbol{\mu}_\ell^T \frac{\partial \mathbf{P}_\ell}{\partial \mathbf{u}_i} + \boldsymbol{\nu}_\ell^T \frac{\partial \mathbf{Q}_\ell}{\partial \mathbf{u}_i} + \frac{\partial J}{\partial \mathbf{u}_i} \right) \cdot \frac{\partial \mathbf{u}_i}{\partial z_e} \\
&\quad + \sum_{i=1}^{N_t} \sum_{\ell=1}^{N_t} \left(\boldsymbol{\xi}_\ell^T \frac{\partial \mathbf{R}_\ell}{\partial \dot{\mathbf{u}}_i} + \boldsymbol{\mu}_\ell^T \frac{\partial \mathbf{P}_\ell}{\partial \dot{\mathbf{u}}_i} + \boldsymbol{\nu}_\ell^T \frac{\partial \mathbf{Q}_\ell}{\partial \dot{\mathbf{u}}_i} \right) \cdot \frac{\partial \dot{\mathbf{u}}_i}{\partial z_e} \\
&\quad + \sum_{i=1}^{N_t} \sum_{\ell=1}^{N_t} \left(\boldsymbol{\xi}_\ell^T \frac{\partial \mathbf{R}_\ell}{\partial \ddot{\mathbf{u}}_i} + \boldsymbol{\mu}_\ell^T \frac{\partial \mathbf{P}_\ell}{\partial \ddot{\mathbf{u}}_i} + \boldsymbol{\nu}_\ell^T \frac{\partial \mathbf{Q}_\ell}{\partial \ddot{\mathbf{u}}_i} \right) \cdot \frac{\partial \ddot{\mathbf{u}}_i}{\partial z_e}.
\end{aligned} \tag{26}$$

If we define $\boldsymbol{\xi}_i$, $\boldsymbol{\mu}_i$, and $\boldsymbol{\nu}_i$ such that all terms containing $\partial\ddot{\mathbf{u}}_i/\partial z_e$, $\partial\dot{\mathbf{u}}_i/\partial z_e$, and $\partial\mathbf{u}_i/\partial z_e$ vanish from (26), then the sensitivity of the AL function simplifies to

$$\frac{\mathrm{d}J^{(k)}}{\mathrm{d}z_e} = \frac{\partial J^{(k)}}{\partial z_e} + \sum_{i=0}^{N_t} \boldsymbol{\xi}_i^T \frac{\partial \mathbf{R}_i}{\partial z_e}. \tag{27}$$

To achieve this simplified form, we define the adjoint problem, such that

$$\boldsymbol{\xi}_0^T \frac{\partial \mathbf{R}_0}{\partial \ddot{\mathbf{u}}_0} + \boldsymbol{\xi}_1^T \frac{\partial \mathbf{R}_1}{\partial \ddot{\mathbf{u}}_0} + \boldsymbol{\mu}_1^T \frac{\partial \mathbf{P}_1}{\partial \ddot{\mathbf{u}}_0} + \boldsymbol{\nu}_1^T \frac{\partial \mathbf{Q}_1}{\partial \ddot{\mathbf{u}}_0} = \mathbf{0} \tag{28}$$

for $i = 0$ and

$$\begin{aligned}
&\sum_{\ell=1}^{N_t} \left(\boldsymbol{\xi}_\ell^T \frac{\partial \mathbf{R}_\ell}{\partial \mathbf{u}_i} + \boldsymbol{\mu}_\ell^T \frac{\partial \mathbf{P}_\ell}{\partial \mathbf{u}_i} + \boldsymbol{\nu}_\ell^T \frac{\partial \mathbf{Q}_\ell}{\partial \mathbf{u}_i} + \frac{\partial J^{(k)}}{\partial \mathbf{u}_i} \right) = \mathbf{0}, \\
&\sum_{\ell=1}^{N_t} \left(\boldsymbol{\xi}_\ell^T \frac{\partial \mathbf{R}_\ell}{\partial \dot{\mathbf{u}}_i} + \boldsymbol{\mu}_\ell^T \frac{\partial \mathbf{P}_\ell}{\partial \dot{\mathbf{u}}_i} + \boldsymbol{\nu}_\ell^T \frac{\partial \mathbf{Q}_\ell}{\partial \dot{\mathbf{u}}_i} \right) = \mathbf{0}, \quad \text{and} \\
&\sum_{\ell=1}^{N_t} \left(\boldsymbol{\xi}_\ell^T \frac{\partial \mathbf{R}_\ell}{\partial \ddot{\mathbf{u}}_i} + \boldsymbol{\mu}_\ell^T \frac{\partial \mathbf{P}_\ell}{\partial \ddot{\mathbf{u}}_i} + \boldsymbol{\nu}_\ell^T \frac{\partial \mathbf{Q}_\ell}{\partial \ddot{\mathbf{u}}_i} \right) = \mathbf{0}
\end{aligned} \tag{29}$$

for $i = 1, \ldots, N_t$.

To solve the adjoint system (28)–(29), we use (14), (23), and (24) to obtain:

$$\boldsymbol{\mu}_{N_t} = \frac{\partial J^{(k)}}{\partial \mathbf{u}_{N_t}}, \quad \boldsymbol{\nu}_{N_t} = \mathbf{0}, \quad \mathbf{M}_1 \boldsymbol{\xi}_{N_t} = -\beta \Delta t^2 \boldsymbol{\mu}_{N_t} - \gamma \Delta t \boldsymbol{\nu}_{N_t} \tag{30}$$

for $i = N_t$,

$$\begin{aligned}
\boldsymbol{\mu}_{i-1} &= \frac{\partial J^{(k)}}{\partial \mathbf{u}_{i-1}} + \mathbf{K}\boldsymbol{\xi}_i + \boldsymbol{\mu}_i, \quad \boldsymbol{\nu}_{i-1} = \mathbf{C}_0 \boldsymbol{\xi}_i + \Delta t \boldsymbol{\mu}_i + \boldsymbol{\nu}_i, \\
\mathbf{M}_1 \boldsymbol{\xi}_{i-1} &= \mathbf{M}_0 \boldsymbol{\xi}_i - \Delta t^2 \left[\beta \boldsymbol{\mu}_{i-1} + \left(\frac{1}{2} - \beta \right) \boldsymbol{\mu}_i \right] \\
&\quad - \Delta t \left[\gamma \boldsymbol{\nu}_{i-1} + (1-\gamma) \boldsymbol{\nu}_i \right]
\end{aligned} \tag{31}$$

for $i = 1, \ldots, N_t - 1$, and

$$\mathbf{M}\boldsymbol{\xi}_0 = \mathbf{M}_0 \boldsymbol{\xi}_1 - \left(\frac{1}{2} - \beta \right) \Delta t^2 \boldsymbol{\mu}_1 - (1-\gamma) \Delta t \boldsymbol{\nu}_1 \tag{32}$$

for $i = 0$.

To solve the adjoint problem, we require the value of $\partial J^{(k)}/\partial \mathbf{u}_i$, $i = 1, \ldots, N_t$, which we obtain from the expression of $J^{(k)}(\mathbf{z}, \mathbf{u}_0, \ldots, \mathbf{u}_{N_t})$ in (16). That is,

$$\frac{\partial J^{(k)}}{\partial \mathbf{u}_i} = \frac{1}{N N_t} \sum_{\ell=1}^{N} \left[\lambda_{\ell i}^{(k)} + \mu_{\ell i}^{(k)} h_{\ell i} \right] \frac{\partial h_{\ell i}}{\partial \mathbf{u}_i} \tag{33}$$

where

$$\frac{\partial h_{\ell i}}{\partial \mathbf{u}_i} = \begin{cases} \mathbf{0}, & \text{if } g_{\ell i} < -\dfrac{\lambda_{\ell i}^{(k)}}{\mu_{\ell i}^{(k)}} \text{ and} \\ \dfrac{\partial g_{\ell i}}{\partial \mathbf{u}_i}, & \text{otherwise.} \end{cases} \tag{34}$$

The non-zero expression for $\partial h_{\ell i}/\partial \mathbf{u}_i$ can be computed in an element-wise manner as

$$\frac{\partial h_{\ell i}}{\partial \mathbf{u}_{\ell i}} = \widetilde{m}_E(y_\ell)(3\Lambda_{\ell i}^2 + 1) \frac{1}{\sigma_{\lim}} \frac{\partial \sigma_{\ell i}^v}{\partial \mathbf{u}_{\ell i}}, \tag{35}$$

where $\mathbf{u}_{\ell i}$ is the displacement vector of element ℓ at time step i and

$$\frac{\partial \sigma_{\ell i}^v}{\partial \mathbf{u}_{\ell i}} = \left(\frac{\partial \boldsymbol{\sigma}_{\ell i}}{\partial \mathbf{u}_{\ell i}} \right)^T \frac{\partial \sigma_{\ell i}^v}{\partial \boldsymbol{\sigma}_{\ell i}} = (\mathbf{D}_0 \mathbf{B}_\ell)^T \frac{\mathbf{V}_0 \boldsymbol{\sigma}_{\ell i}}{\sigma_{\ell i}^v}. \tag{36}$$

The use of the volume interpolation function, $m_V(\mathbf{y})$, and the stiffness interpolation function, $m_E(\mathbf{y})$, requires that we rewrite (27) using the chain rule:

$$\frac{\mathrm{d}J^{(k)}}{\mathrm{d}z_e} = \sum_{\ell=1}^{N} \left(\frac{\partial E_\ell}{\partial z_e} \frac{\mathrm{d}J^{(k)}}{\mathrm{d}E_\ell} + \frac{\partial V_\ell}{\partial z_e} \frac{\mathrm{d}J^{(k)}}{\mathrm{d}V_\ell} \right), \tag{37}$$

where $\mathbf{V} = \widetilde{m}_V(\mathbf{y})$ and $\mathbf{E} = \widetilde{m}_E(\mathbf{y})$ are vectors containing the volume and stiffness interpolation function values for all elements, respectively, and

$$\begin{aligned}
\frac{\mathrm{d}J^{(k)}}{\mathrm{d}E_\ell} &= \frac{\partial J^{(k)}}{\partial E_\ell} + \sum_{i=0}^{N_t} \boldsymbol{\xi}_i^T \frac{\partial \mathbf{R}_i}{\partial E_\ell} \quad \text{and} \\
\frac{\mathrm{d}J^{(k)}}{\mathrm{d}V_\ell} &= \frac{\partial J^{(k)}}{\partial V_\ell} + \sum_{i=0}^{N_t} \boldsymbol{\xi}_i^T \frac{\partial \mathbf{R}_i}{\partial V_\ell}.
\end{aligned} \tag{38}$$

We write (37) more compactly as

$$\frac{\mathrm{d}J^{(k)}}{\mathrm{d}\mathbf{z}} = \frac{\partial \mathbf{E}}{\partial \mathbf{z}} \frac{\mathrm{d}J^{(k)}}{\mathrm{d}\mathbf{E}} + \frac{\partial \mathbf{V}}{\partial \mathbf{z}} \frac{\mathrm{d}J^{(k)}}{\partial \mathbf{V}}, \tag{39}$$

where

$$\frac{\partial \mathbf{E}}{\partial \mathbf{z}} = \mathbf{P}^T J_{m_E}(\mathbf{y}) \quad \text{and} \quad \frac{\partial \mathbf{V}}{\partial \mathbf{z}} = \mathbf{P}^T J_{m_V}(\mathbf{y}), \tag{40}$$

with $J_{m_E} = \mathrm{diag}(\widetilde{m}_E'(y_1), \ldots, \widetilde{m}_E'(y_N))$ and $J_{m_V} = \mathrm{diag}(\widetilde{m}_V'(y_1), \ldots, \widetilde{m}_V'(y_N))$.

To obtain the terms $\partial \mathbf{R}_i/\partial E_\ell$ and $\partial \mathbf{R}_i/\partial V_\ell$ in (38), we use (23) for $i = 0$ and obtain

$$\begin{aligned}
\frac{\partial \mathbf{R}_i}{\partial E_\ell} &= \frac{\partial \mathbf{K}}{\partial E_\ell} (\mathbf{u}_0 + \beta_r \dot{\mathbf{u}}_0) = \mathbf{k}_\ell (\mathbf{u}_{\ell 0} + \beta_r \dot{\mathbf{u}}_{\ell 0}) \quad \text{and} \\
\frac{\partial \mathbf{R}_i}{\partial V_\ell} &= \frac{\partial \mathbf{M}}{\partial V_\ell} (\ddot{\mathbf{u}}_0 + \alpha_r \dot{\mathbf{u}}_0) = \mathbf{m}_\ell (\ddot{\mathbf{u}}_{\ell 0} + \alpha_r \dot{\mathbf{u}}_{\ell 0}).
\end{aligned} \tag{41}$$

Likewise, we use (14) for $i = 1, \ldots, N_t$ and obtain

$$\begin{aligned}
\frac{\partial \mathbf{R}_i}{\partial E_\ell} &= \frac{\partial \mathbf{K}}{\partial E_\ell} \left[(1-\alpha)(\mathbf{u}_i + \beta_r \dot{\mathbf{u}}_i) + \alpha(\mathbf{u}_{i-1} + \beta_r \dot{\mathbf{u}}_{i-1}) \right] \\
&= \mathbf{k}_\ell \left[(1-\alpha)(\mathbf{u}_{\ell i} + \beta_r \dot{\mathbf{u}}_{\ell i}) + \alpha(\mathbf{u}_{\ell,i-1} + \beta_r \dot{\mathbf{u}}_{\ell,i-1}) \right] \quad \text{and} \\
\frac{\partial \mathbf{R}_i}{\partial V_\ell} &= \frac{\partial \mathbf{M}}{\partial V_\ell} \left[\ddot{\mathbf{u}}_i + \alpha_r \left((1-\alpha) \dot{\mathbf{u}}_i + \alpha \dot{\mathbf{u}}_{i-1} \right) \right] \\
&= \mathbf{m}_\ell \left[\ddot{\mathbf{u}}_{\ell i} + \alpha_r \left((1-\alpha) \dot{\mathbf{u}}_{\ell i} + \alpha \dot{\mathbf{u}}_{\ell,i-1} \right) \right].
\end{aligned} \tag{42}$$

We use double subscripts (ℓi) or $(\ell, i-1)$ in (41) and (42) to refer to element-wise quantities (i.e., vectors of elemental displacements, velocities, or accelerations).

Finally, we use the AL function in (16) to obtain $\partial J^{(k)}/\partial E_\ell$ and $\partial J^{(k)}/\partial V_\ell$ in (37) and obtain:

$$\frac{\partial J^{(k)}}{\partial E_\ell} = \frac{1}{NN_t}\sum_{i=0}^{N_t}\sum_{\ell=1}^{N}\left[\lambda_{\ell i}^{(k)} + \mu_{\ell i}^{(k)} h_{\ell i}\right]\frac{\partial h_{\ell i}}{\partial E_\ell} \quad \text{and}$$

$$\frac{\partial J^{(k)}}{\partial V_\ell} = \frac{A_\ell}{\mathbf{A}^T\mathbf{1}} + \frac{1}{NN_t}\sum_{i=0}^{N_t}\sum_{\ell=1}^{N}\left[\lambda_{\ell i}^{(k)} + \mu_{\ell i}^{(k)} h_{\ell i}\right]\frac{\partial h_{\ell i}}{\partial V_\ell}, \quad (43)$$

where the first term of $\partial J^{(k)}/\partial V_\ell$ comes from the definition of $f(\mathbf{z})$ in (1). Because $h_{\ell i}$ has no explicit dependence on V_ℓ (see (17)), then $\partial h_{\ell i}/\partial V_\ell = 0$. However, $h_{\ell i}$ depends explicitly on E_ℓ, as shown in $(1)_2$ and (17). Thus, we use (17), with $g_{\ell i}(\mathbf{z}, \mathbf{u}_i) = E_\ell \Lambda_{\ell i}(\Lambda_{\ell i}^2 + 1)$ from $(1)_2$, and obtain $\partial h_{\ell i}/\partial E_\ell$ as follows:

$$\frac{\partial h_{\ell i}}{\partial E_\ell} = \begin{cases} 0, & \text{if } g_{\ell i} < -\dfrac{\lambda_{\ell i}^{(k)}}{\mu_{\ell i}^{(k)}} \text{ and} \\ \Lambda_{\ell i}(\Lambda_{\ell i}^2 + 1), & \text{otherwise.} \end{cases} \quad (44)$$

6 Some implementation details

The implementation of the dynamic, stress-constrained topology optimization formulation introduced previously follows the schematic flowchart shown in Fig. 1. The first step is to read all necessary input data, including the finite element discretization and boundary conditions, initial values for $\lambda_{\ell i}^{(k)}$ and $\mu_{\ell i}^{(k)}$, initial density distribution, $\mathbf{z}^{(0)}$, parameters for the optimizer, and convergence tolerances. Using the provided input data, the next step is to use the method of moving asymptotes (MMA) to find an approximate minimizer of the k-th AL sub-problem (16). A flowchart describing the main steps required to find the approximate minimizer of the k-th AL sub-problem is shown on the right-hand side of Fig. 1. Once the approximate minimizer, $\mathbf{z}^{(k)}$, has been obtained, the next step is to update the Lagrange multiplier estimators, $\lambda_{\ell i}^{(k+1)}$, and the quadratic penalty terms, $\mu_{\ell i}^{(k+1)}$, as shown in (18) and (19), respectively. This process is repeated until some convergence criteria are satisfied. We determine that the solution has converged if $\frac{1}{N}\text{sum}(|\mathbf{z}_{i+1}^{(k)} - \mathbf{z}_i^{(k)}|) \leq \texttt{Tol}$ and $\|\widetilde{\boldsymbol{\sigma}}^v\|_\infty - 1 \leq \texttt{TolS}$, where `Tol` and `TolS` are prescribed tolerances, or if k has reached a maximum number of iterations, `MaxIter`.

6.1 Solution of the AL sub-problems

We use MMA to solve the AL sub-problems (see flowchart on the right-hand side of Fig. 1), for which we need to evaluate the sensitivity $\partial J^{(k)}/\partial \mathbf{z}$ of the AL function. The Algorithm 1 contains a pseudo-code with the main steps required to evaluate $J^{(k)}$ and $\partial J^{(k)}/\partial \mathbf{z}$ in order to update

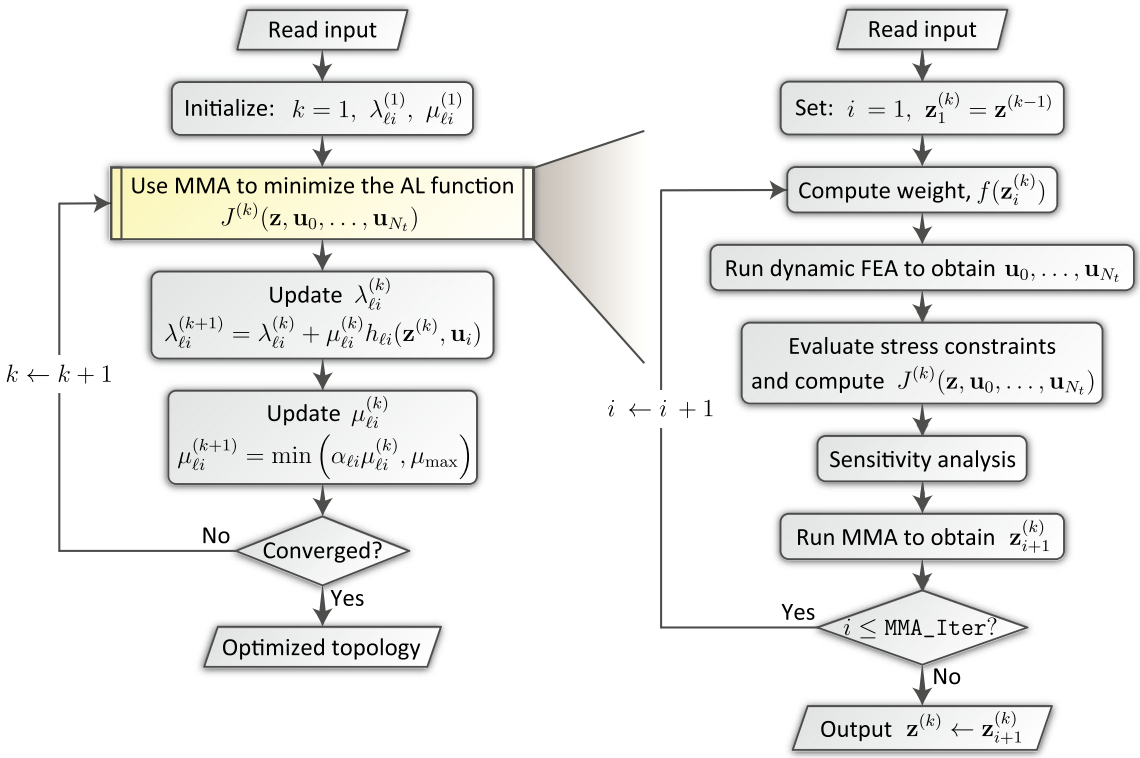

Fig. 1 Schematic flowchart of the AL-based framework introduced to solve dynamic, stress-constrained topology optimization problems

the design variables, and thus, solve each AL sub-problem. We solve the AL sub-problems in an approximate way by running a small number, `MMA_Iter`, of MMA iterations. Running a few MMA iterations per AL sub-problem proved effective in solving quasi-static stress-constrained topology optimization problems (Senhora et al. 2020; Giraldo-Londoño and Paulino 2020, 2021b) and has also proven effective to solve the problem in the dynamic setting. To facilitate the implementation of the dynamic, stress-constrained formulation introduced herein, the interested reader is referred to Giraldo-Londoño and Paulino (2021a) for a Matlab implementation of the HHT-α method (line 4 of Algorithm 1) and that of the adjoint problem (line 10 of Algorithm 1), and to Giraldo-Londoño and Paulino (2021b) for a Matlab implementation of the AL-based formulation in the quasi-static setting.

Algorithm 1 Solution of the k-th AL sub-problem (16).

1: Set $i = 1$ and $\mathbf{z}_1^{(k)} = \mathbf{z}^{(k-1)}$
2: **for** i=1 to `MMA_Iter` **do**
3: Evaluate objective function, $f(\mathbf{z}_i^{(k)}) = \mathbf{A}^T m_V(\mathbf{y})/(\mathbf{A}^T\mathbf{1})$, as shown in (1), with $\mathbf{y} = \mathbf{P}\mathbf{z}_i^{(k)}$
4: Use the HHT-α method, as discussed in Section 3, to obtain $\mathbf{u}_0, \ldots, \mathbf{u}_{N_t}$
5: Using $\mathbf{u}_0, \ldots, \mathbf{u}_{N_t}$, compute the von Mises stresses, $\sigma_{\ell i}^v$, as shown in (10)–(11)
6: Evaluate the stress constraints, $g_{\ell i}(\mathbf{z}, \mathbf{u}_i) = \widetilde{m}_E(y_\ell)\Lambda_{\ell i}(\Lambda_{\ell i}^2 + 1)$, with $\Lambda_{\ell i}$ as given in (9)
7: Compute $h_{\ell i}(\mathbf{z}, \mathbf{u}_i)$ as shown in (17)
8: Evaluate the AL function, $J^{(k)}(\mathbf{z}, \mathbf{u}_0, \ldots, \mathbf{u}_{N_t})$, as shown in (16)
9: Solve the adjoint problem (30)–(32) to find $\boldsymbol{\xi}_0, \ldots, \boldsymbol{\xi}_{N_t}$
10: Use adjoint variables $\boldsymbol{\xi}_0, \ldots, \boldsymbol{\xi}_{N_t}$ to find $\mathrm{d}J^{(k)}/\mathrm{d}E_\ell$ and $\mathrm{d}J^{(k)}/\mathrm{d}V_\ell$ as shown in (38)
11: Use the values of $\mathrm{d}J^{(k)}/\mathrm{d}E_\ell$ and $\mathrm{d}J^{(k)}/\mathrm{d}V_\ell$ to computed $J^{(k)}/\mathrm{d}\mathbf{z}$, as shown in (39)
12: Use $\mathrm{d}J^{(k)}/\mathrm{d}\mathbf{z}$ to find $\mathbf{z}_{i+1}^{(k)}$ with the MMA version discussed in Section 6.2 and in Appendix A
13: **if** $(\mathrm{sum}(|\mathbf{z}_{i+1}^k - \mathbf{z}_i^k|)/N <$ `Tol` and $\max(\tilde{\boldsymbol{\sigma}}^v) - 1 \leq$ `TolS`$)$ **then**
14 : Exit loop
15 : **end if**
16 : **end if**
17 : Set $\mathrm{z}^{(k)} \leftarrow \mathbf{z}_{i+1}^{(k)}$
18: Return $\mathbf{z}^{(k)}$

6.2 Specialized MMA version

We update the design variables using a version of the method of moving asymptotes (MMA) (Svanberg 1987) especially designed to solve the AL optimization problem. We use this simplification because each AL sub-problem is in practice, an unconstrained optimization problem. At each AL step, k, we approximate the AL sub-problem (16) with the approach discussed in Appendix A.

7 Results and discussion

This section presents several numerical examples to elucidate the ability of the AL-based framework to solve dynamic, stress-constrained topology optimization problems. Specifically, we solve four two-dimensional design problems that explore different dynamic loading scenarios, including loads that are fixed at a point and vary in magnitude and/or direction, and loads that are fixed in magnitude and move in space. To solve all problems, we use the set of default input parameters shown in Table 1.[6]

7.1 L-bracket design under a rotating load

This example deals with the design of an L-bracket subjected to a load of magnitude P that rotates at a prescribed angular frequency, ω, as depicted in Fig. 2 (left). We design the L-bracket assuming that the load rotates three times and, to avoid large dynamic amplification effects, we use a load $f(t)$ which we ramp linearly from $f(t) = 0$ at $t = 0$ to $f(t) = P$ at $t = \pi/(2\omega)$ (i.e., at the first quarter cycle), as shown in Fig. 2 (right). The L-bracket is one of the typical benchmark problems found in the stress constraints literature (e.g., see Pereira et al. 2004; Bruggi 2008; Paris

[6]The numerical results presented in this section were obtained using a Matlab implementation of the proposed formulation running on a computer with an i7-4930k CPU at 3.40 GHz and 256 GB of RAM running on a 64-bit operating system.

Table 1 Input parameters used to solve all examples

Initial Lagrange multiplier estimators, $\lambda_{\ell i}^{(1)}$	0
Initial penalty factors, $\mu_{\ell i}^{(1)}$	10
Maximum penalty factor, $\mu_{\max}$	200,000
Penalty factor update parameter, $\tilde{\alpha}$	1.05
RAMP penalization factor, p_0	6
Nonlinear filter exponent, q	3
Ersatz parameter, ϵ	10^{-6}
MMA iterations per AL step, `MMA_Iter`	10
Initial threshold projection penalization factor, $\bar{\beta}^{\dagger}$	1
Maximum threshold projection penalization factor, $\bar{\beta}_{\max}^{\dagger}$	12
Threshold projection density, $\bar{\eta}$	0.5
Initial guess, $\mathbf{z}^{(0)}$	0.5
Convergence tolerance on design variables, `Tol`	0.00075
Convergence tolerance on stress constraints, `TolS`	0.007
Maximum number of AL steps, `MaxIter`	100

†Parameter $\bar{\beta}$ starts at 1 and increases by 2 every two AL steps and up to the maximum value, $\bar{\beta}_{\max}$

Table 2 Input parameters for the L-bracket

L-bracket length, L	1 m
L-bracket thickness, h_0	1 m
Applied load, P	1.5×10^6 N
Load distribution length, d	0.06 m
Young's modulus of solid material, E_0	70 GPa
Poisson's ratio of solid material, ν_0	0.3
Mass density of solid material, ρ_0	2700 kg/m^3
Stress limit, σ_{lim}	100 MPa
Simulation time, $T_{\max}$	$6\pi/\omega$
Number of time steps, N_t	75
Rayleigh damping parameters, α_r and β_r	$[10,\ 1 \times 10^{-5}]$
Filter radius and filter exponent, R and q	0.05 m and 3

et al. 2009, 2010; Amstutz and Novotny 2010; Le et al. 2010; Guo et al. 2011; Bruggi and Duysinx 2012; Holmberg et al. 2013a, b; Emmendoerfer Jr and Fancello 2014, 2016). To facilitate reproduction of the results, Table 2 displays all additional input parameters used for the design.

Using a regular mesh with 29,584 Q4 elements generated with `PolyMesher` (Talischi et al. 2012a), we obtain the results shown in Fig. 3 for various values of ω. The top figures display the optimized topologies of the L-bracket and the bottom ones the envelope of von Mises stress during the entire loading time. The envelope of von Mises stress for each element is computed as the maximum von Mises stress of that element for all time steps. As shown by the stress maps, the AL-based framework renders optimized topologies that satisfy the stress constraints locally at every point of the design domain and for every time step of the dynamic analysis. The results also show that the optimized designs depend on the value of ω, leading to structures with larger volume fractions as ω increases. The increase in volume fraction as ω increases is expected because inertial forces become more dominant as the load changes direction at a faster rate, which leads to increased von Mises stress as compared to a static-like situation. One can also observe that the complexity of the lateral bracing system of the L-bracket increases when $\omega \geq 100\pi$ rad/s. The increase in complexity is expected to happen in order to prevent excessive horizontal deflections when the dynamic effects become relevant. To verify that the input parameters from Table 1 are suitable to solve the stress-constrained problem independently of the number of constraints, we solved the L-bracket problem for $\omega = 5\pi$ rad/s with $N_t = 750$ and $N_t = 7500$, which corresponds to $NN_t = 20.2 \times 10^6$ and $NN_t = 202 \times 10^6$ stress constraints, respectively, and obtained consistent results in both cases.

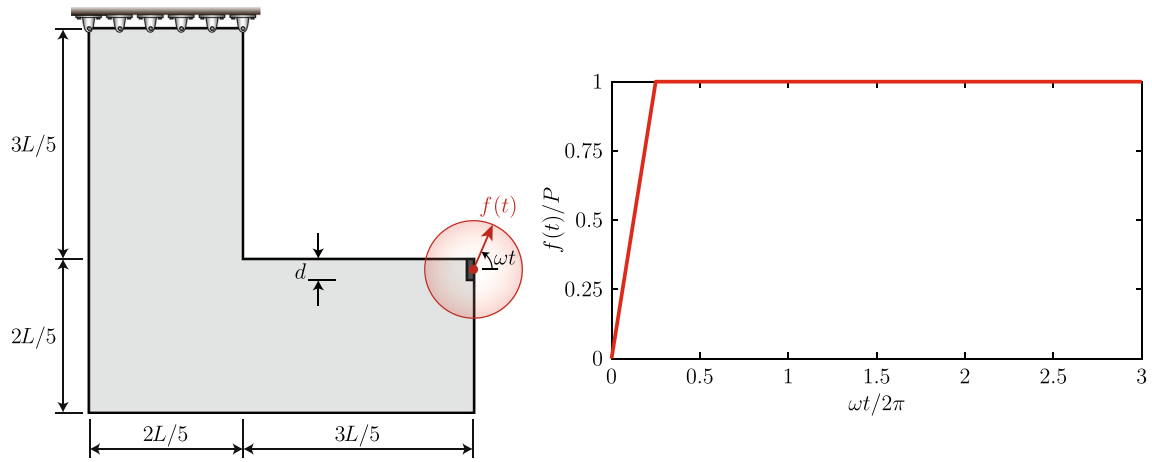

Fig. 2 L-bracket subjected to a load, $f(t)$, rotating at a prescribed angular velocity, ω. To avoid excessive dynamic amplification effects, we ramp $f(t)$ linearly from 0 at $t = 0$ to P at $t = \pi/(2\omega)$

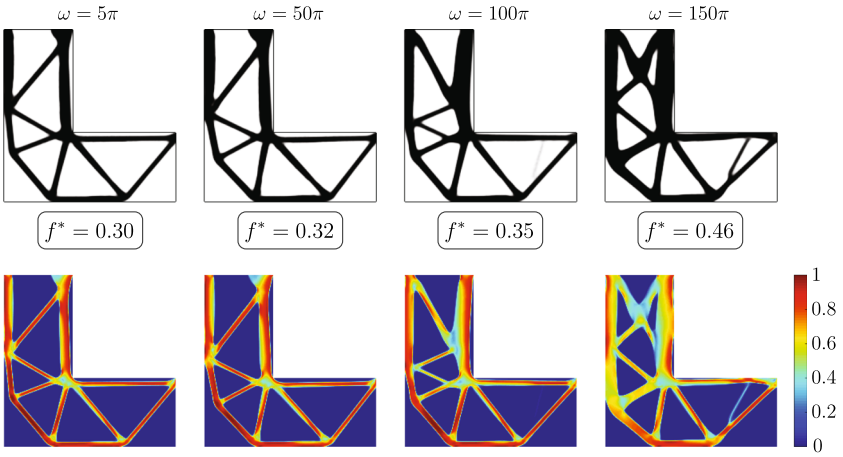

Fig. 3 Optimized topologies (top) and von Mises stress envelopes (bottom) of the L-bracket for various frequencies, ω (rad/s). The values of f^* correspond to the optimized volume fractions, $f(\mathbf{z}^*)$, for each design

To visualize the evolution of von Mises stress during the loading history, Fig. 4 depicts the deformed shapes of the optimized topologies form Fig. 3 at various instances in time. As shown by these results, different members of the optimized designs reach the stress limit at different instances in time. For example, for $T = 0.25T_{\max}$ and $T = 0.75T_{\max}$, the overall tendency is for both the bottom chord and the region near the re-entrant corner of the bracket to reach the stress limit, and for $T = 0.50T_{\max}$ and $T = T_{\max}$, the general tendency is for the diagonal

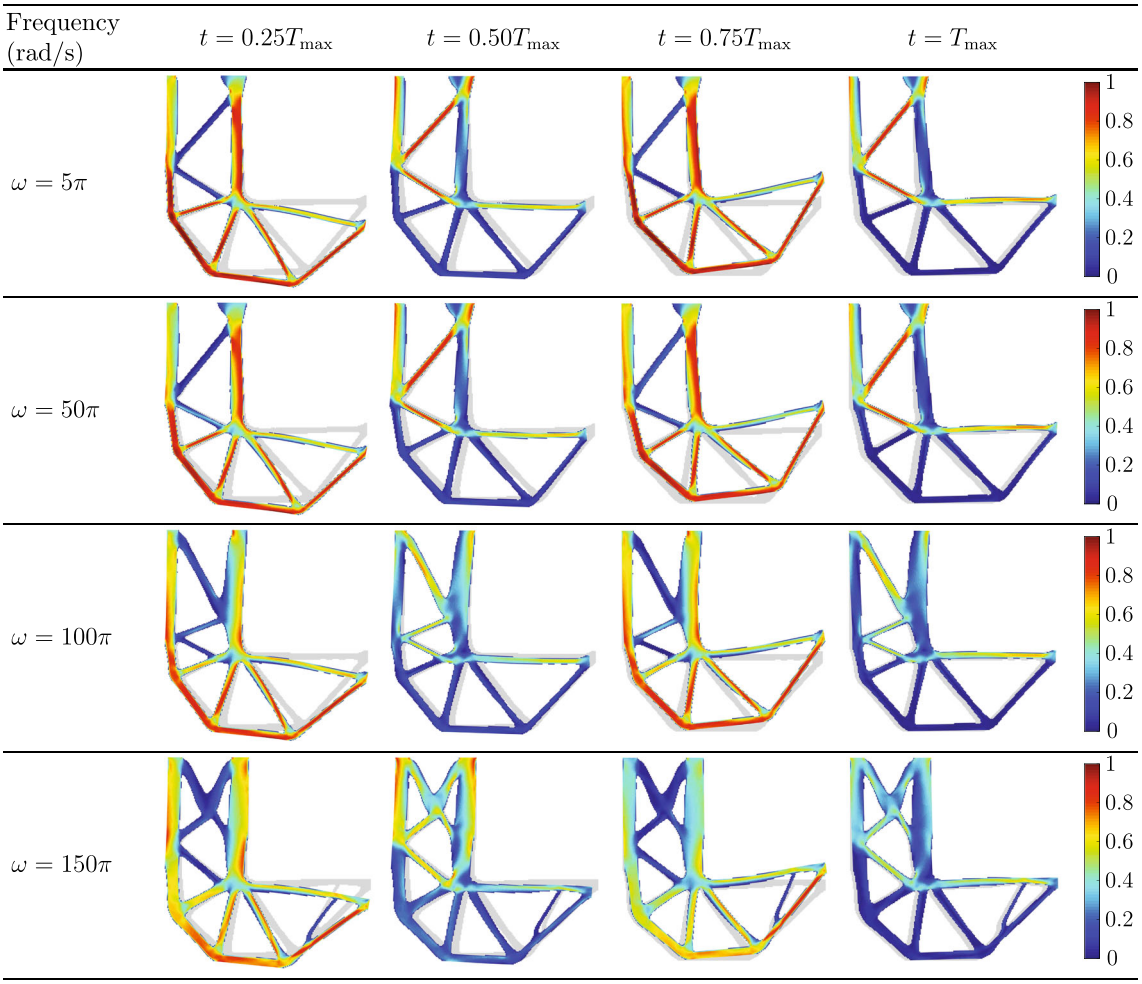

Fig. 4 Snapshots of von Mises stress maps at various instances in time for the designs from Fig. 3

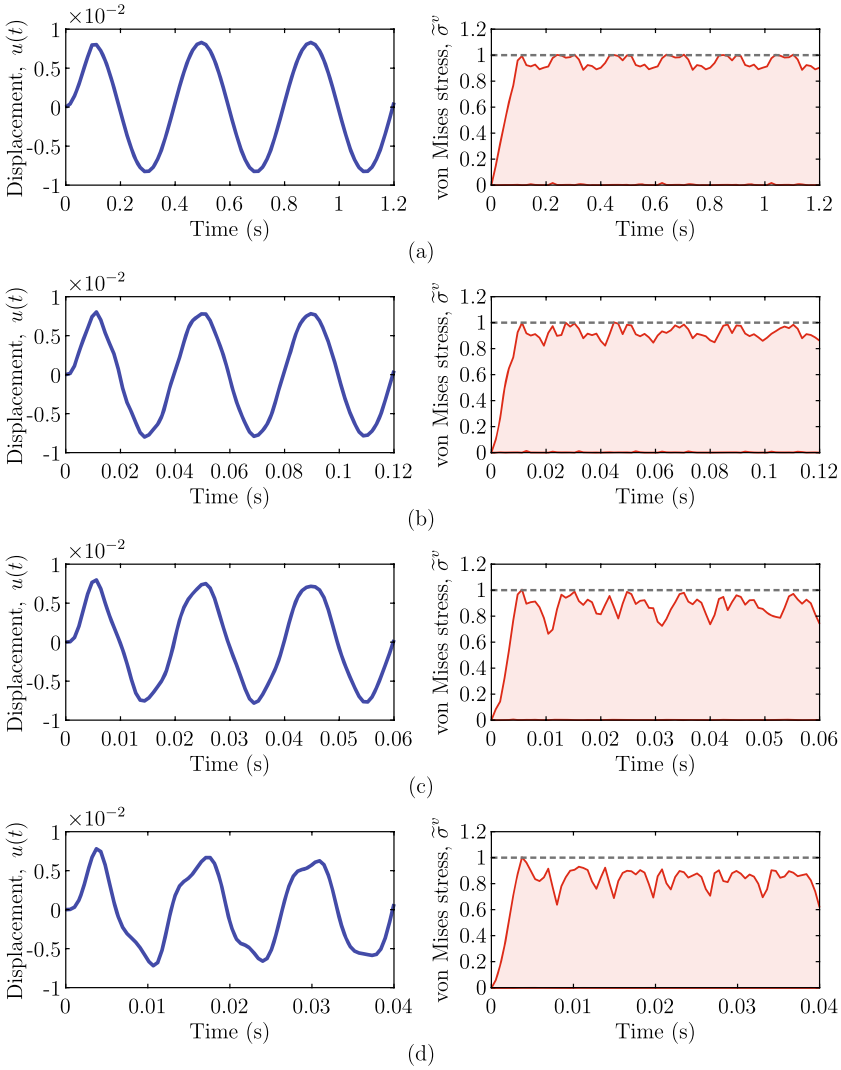

Fig. 5 Time histories of horizontal displacements at the load application point (left) and of maximum and minimum von Mises stress values (right) corresponding to the designs of Fig. 3: (a) $\omega = 5\pi$ rad/s, (b) $\omega = 50\pi$ rad/s, (c) $\omega = 100\pi$ rad/s, and (d) $\omega = 150\pi$ rad/s

members at the upper part of the bracket to reach the stress limit. The bottom chord and the members attached to the re-entrant corner become highly stressed when the bracket deforms mainly vertically and the diagonal member a the upper part becomes highly stressed when the bracket deforms horizontally. This means that optimized designs are effective to restrict the movement of the bracket in all directions, which is consistent with the rotating load acting on the bracket.

To have a more complete view of the dynamic behavior of the optimized L-brackets, we display the time history of horizontal displacements at one of the nodes where the load is applied as well as the time history of maximum and minimum von Mises stresses in the entire design domain.[7]

[7]To obtain the von Mises stresses shown in Fig. 5 (right) and in similar figures hereafter, we only select the elements with density greater than or equal to 0.5.

As shown by the results in Fig. 5 (left), the dynamic effects become more notorious as ω increases. The results in Fig. 5 (right) verify that the formulation indeed satisfies the stress constraints throughout the entire duration of the dynamic loading.

7.2 Double corbel design under dynamic vehicular loads

In this example, we design a double corbel whose geometry and boundary conditions are depicted in Fig. 6. The corbel is subjected to two dynamic loads, $f_1(t)$ and $f_2(t)$, which are intended to simulate dynamic vehicular loads, $L(t)$, in addition to the dead weight of the deck supported by the corbel, $D(t)$. For simplicity, we assume that the vehicular loads are given by a sinusoidal function and apply the dead load linearly between $t = 0$ and $t = \pi/(2\omega)$, similarly to the way load $f(t)$ was imposed in the previous example. We

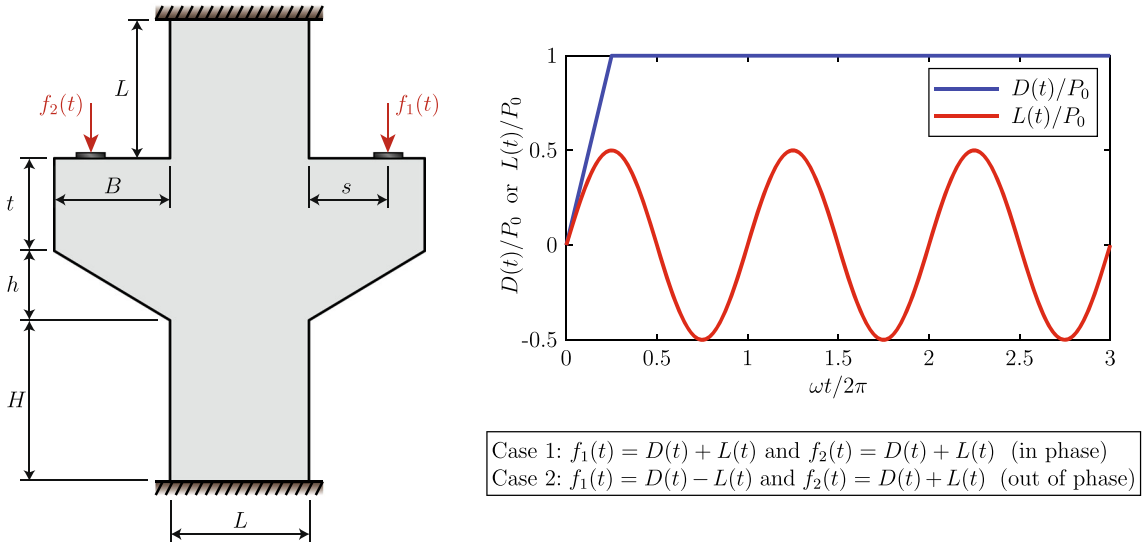

Fig. 6 Double corbel subjected to dynamic loads, $f_1(t)$ and $f_2(t)$ (left), and their explicit time history (right)

consider two loading scenarios, one in which the loads are in phase (i.e., $f_1(t) = f_2(t) = D(t) + L(t)$) and one in which the loads are out of phase (i.e., $f_1(t) = D(t) - L(t)$ and $f_2(t) = D(t) + L(t)$). We include the second loading scenario to investigate the effect of the rotation induced to the structure by the out-of-phase loads.

To facilitate reproduction of the results, Table 3 provides relevant input parameters related to the corbel geometry, loading, material properties, among others. As shown in the table, we use material properties for steel, which is because the purpose of this example is to find the optimized distribution of reinforcement within the corbel. Finally, although the corbel geometry is symmetric, one cannot guarantee to obtain symmetric topologies, and thus, we enforce symmetry to the space of density fields with respect to the vertical axis (Giraldo-Londoño and Paulino 2021b).

Table 3 Input parameters for the double corbel

Dimension, L	0.30 m
Dimension, H	0.35 m
Dimension, h	0.15 m
Dimension, t	0.20 m
Dimension, B	0.25 m
Corbel thickness, h_0	0.30 m
Load magnitude, P_0	2.5×10^6 N
Load eccentricity, s	0.20 m
Load distribution length, d	0.05 m
Young's modulus of solid material, E_0	200 GPa
Poisson's ratio of solid material, ν_0	0.3
Mass density of solid material, ρ_0	7800 kg/m^3
Stress limit, σ_{lim}	420 MPa
Simulation time, T_{max}	$6\pi/\omega$
Number of time steps, N_t	75
Rayleigh damping parameters, α_r and β_r	$[5,\ 1 \times 10^{-5}]$
Filter radius and filter exponent, R and q	0.03 m and 3

We design the corbel using a mesh composed of 30,000 polygonal finite elements generated with `PolyMesher` and obtain optimized topologies for various values of ω. Figure 7 displays two sets of results: one for in-phase loading (top) and one for out-of-phase loading (bottom). The results show that the tension members (i.e., the steel reinforcement) are more inclined when the loads are out of phase than when the loads are in phase. That is because the in-phase loading produces more horizontal stresses than out-of-phase loading, leading to more horizontal members developing in the in-phase loading scenario.

The results of Fig. 7 also show that the optimized topology of the corbel is not sensitive to the loading frequency, except for the case in which the frequency is highest (i.e., for $\omega = 500\pi$ rad/s). For that loading frequency, the triangular region on the upper part of the design under in-phase loading shrinks as compared to designs obtained for lower frequencies. Similarly, when $\omega = 500\pi$ rad/s, the design under out-of-phase loading develops a cross member at the center of the corbel, which helps to prevent the increasing rotational effects generated as ω increases. Note that, independently of the type of loading used, the optimized designs of the corbel are unlike traditional corbel designs, which consists mainly of horizontal stirrups. Thus, the designs obtained in this study can serve as a guideline for corbel designs with optimized performance.

The stress maps shown in Fig. 7 are envelopes obtained for the entire loading history. To gain better understanding of the dynamic behavior of the two types of design, Fig. 8

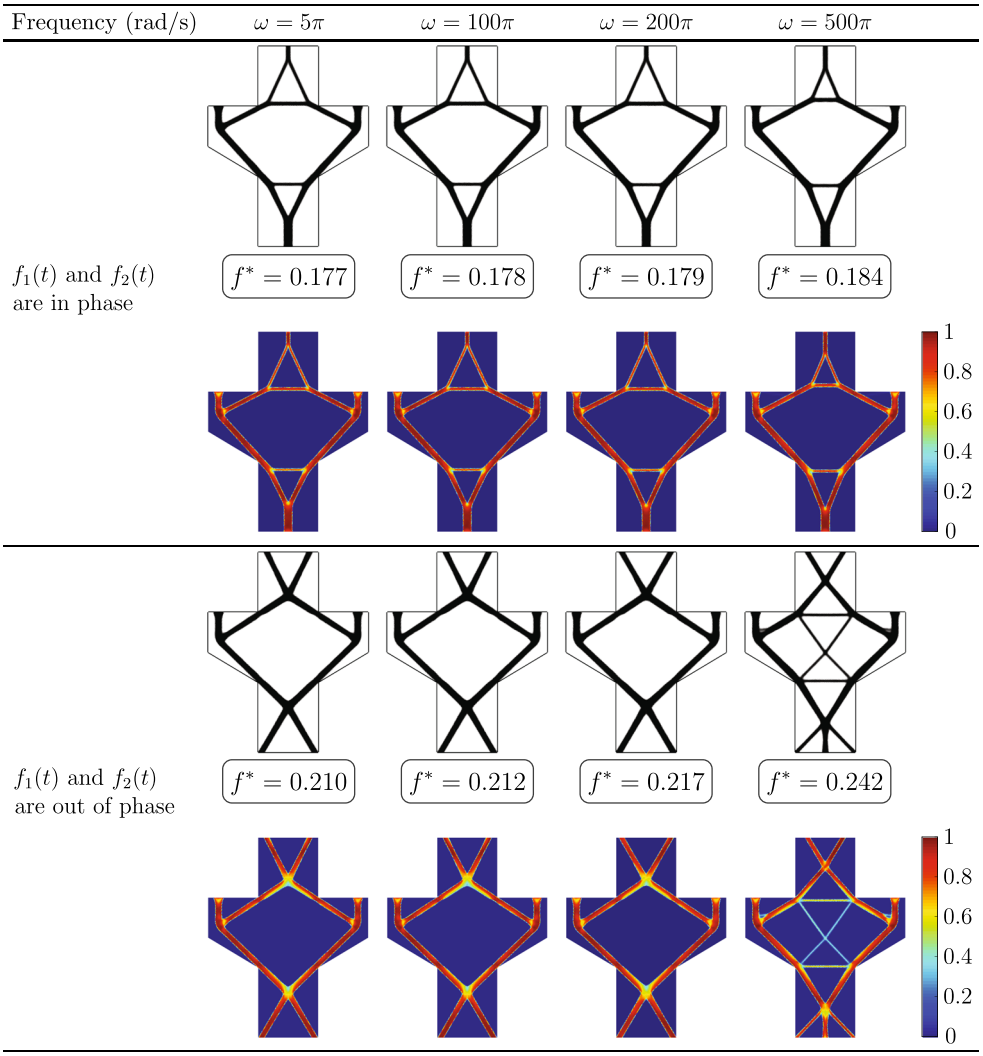

Fig. 7 Double corbel topologies and von Mises stress envelopes obtained for various values of ω (rad/s). The top set of results correspond to the case when $f_1(t)$ and $f_2(t)$ are in phase and the bottom set of results to the case when $f_1(t)$ and $f_2(t)$ are out of phase. The values of f^* correspond to the optimized volume fractions, $f(\mathbf{z}^*)$, for each design

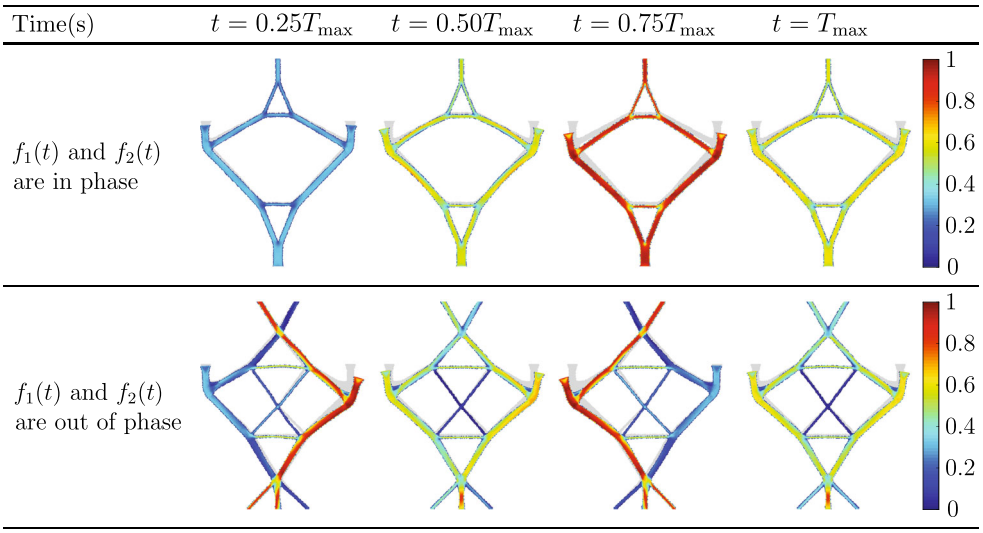

Fig. 8 Snapshots showing the evolution of the von Mises stress maps at various instances in time for the corbels designed for $\omega = 500\pi$ rad/s. The top set of results corresponds to the case in which $f_1(t)$ and $f_2(t)$ are in phase and the bottom set to the case in which $f_1(t)$ and $f_2(t)$ are out of phase

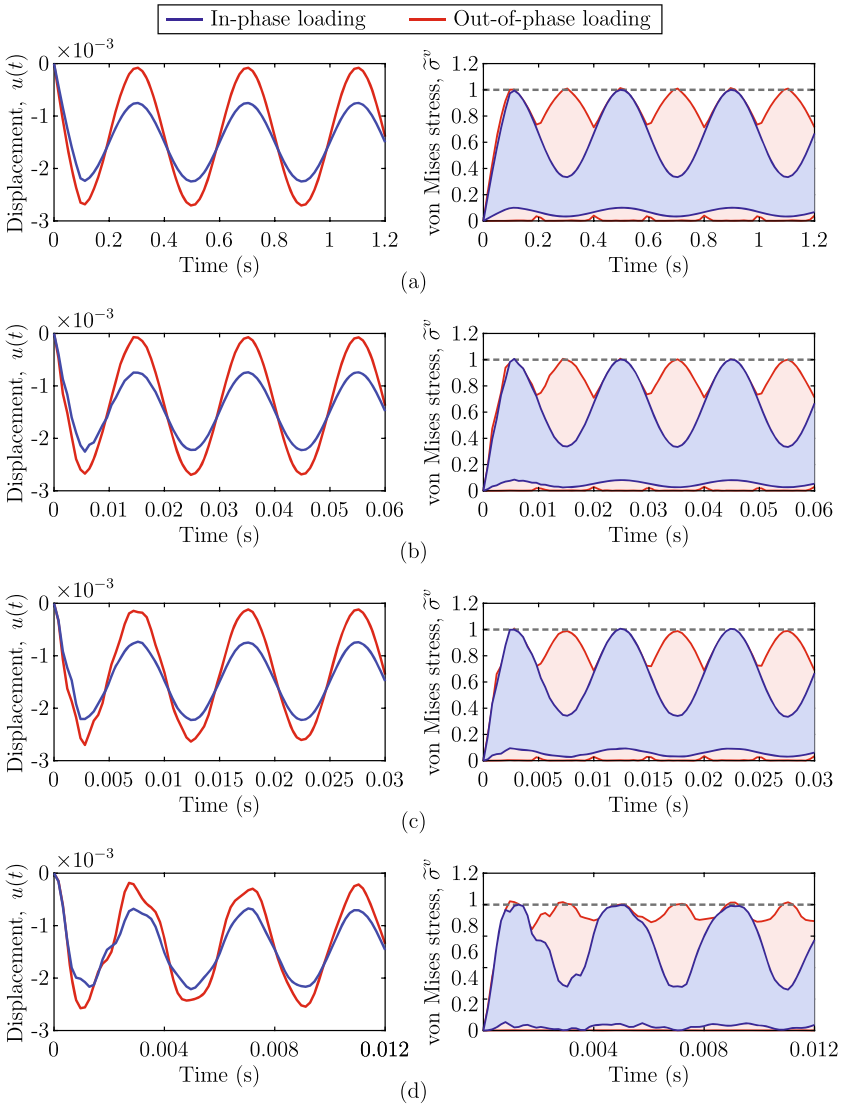

Fig. 9 Dynamic response comparison for the optimized designs of Fig. 7: (**a**) $\omega = 5\pi$ rad/s, (**b**) $\omega = 100\pi$ rad/s, (**c**) $\omega = 200\pi$ rad/s, and (**d**) $\omega = 500\pi$ rad/s. The left set of results displays the time histories of vertical displacements at the point where $f_2(t)$ is applied and the right set of results displays the time histories of minimum and maximum von Mises stress

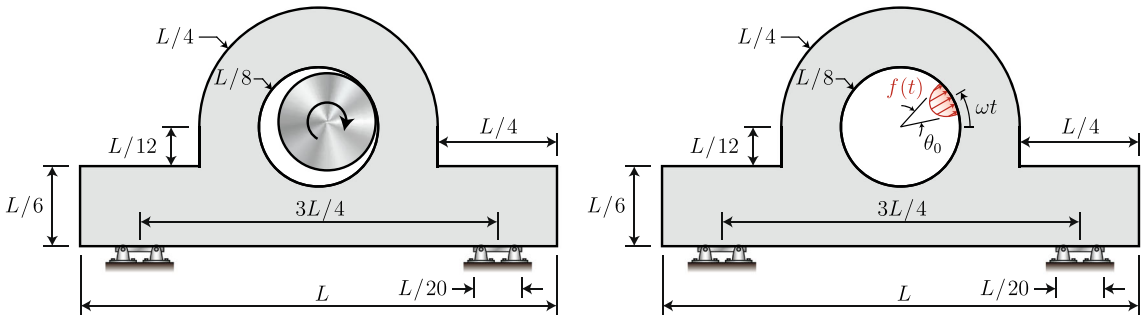

Fig. 10 Pillow bracket domain and boundary conditions. An eccentric shaft rotating at a given angular frequency (left) is represented by a rotating load, $f(t)$, distributed in a nonuniform way over the contact area of the rod (right).We ramp $f(t)$ linearly from $f(t) = 0$ at $t = 0$ $f(t) = P$ at $t = \pi/(2\omega)$

Table 4 Input parameters for the pillow bracket

Pillow bracket width, L	0.1 m
Pillow bracket thickness, h_0	0.05 m
Applied load, P	2×10^4 N
Contact angle, θ_0	30°
Young's modulus of solid material, E_0	70 GPa
Poisson's ratio of solid material, ν_0	0.3
Mass density of solid material, ρ_0	2700 kg/m^3
Stress limit, σ_{lim}	250 MPa
Simulation time, T_{max}	$6\pi/\omega$
Number of time steps, N_t	75
Rayleigh damping parameters, α_r and β_r	$[10,\ 1 \times 10^{-5}]$
Filter radius and filter exponent, R and q	1.5×10^{-3} m and 3

displays the von Mises stress maps for the in-phase design and the out-of-phase design obtained for $\omega = 500\pi$ rad/s at various instances in time. As observed from these results, the stress maps for the design under in-phase loading are symmetric over time. However, the stress maps for the out-of-phase loading are not symmetric and different regions of the structure reach the stress limit at different instances in time.

To compare the dynamic response between the two types of designs, Fig. 9 displays the time history of vertical displacements at the location where $f_2(t)$ is applied as well as the time history of maximum and minimum von Mises stress in the entire design domain. As the results clearly demonstrate, the vertical displacements of the designs under in-phase loading are significantly smaller than those under out-of-phase loading. The larger displacements observed for the out-of-phase designs are expected due to the rocking effect induced by this type of loading, which is not present in the in-phase designs due to their symmetric displacement field (cf. Fig. 8). Although the out-of-phase designs deflect more than the in-phase designs, the von Mises stress histories show that both designs satisfy the stress constraints during the entire loading history.

7.3 Pillow bracket design under a rotating distributed load

This example considers the design of a pillow bracket subjected to a distributed force $f(t)$ that rotates at a given angular frequency, ω, as shown in Fig. 10. This design aims to represent the loading scenario of Fig. 10 (left), in which an eccentric shaft rotates at a given angular frequency, leading to a nonuniform load distribution that changes in position along the inner circle of the bracket. All designs presented in this example assume that the load rotates three times and, as in the first example, the load is increased linearly between $f(t) = 0$ at $t = 0$ and $f(t) = P$ at $t = \pi/(2\omega)$. All input parameters related to this example, including dimensions, loading, and material properties, are displayed in Table 4.

To obtain all designs in this example, we use `PolyMesher` to discretize the design domain using 30,000 polygonal elements and impose symmetry to the space of admissible density fields via a projection approach (Giraldo-Londoño and Paulino 2021b). Figure 11 displays several optimized designs that we obtain for various values of the angular frequency, ω. As shown by these results, it is clear that the optimizer renders designs with a large amount of holes distributed between the inner and the outer circle of the bracket and four slender members connecting the optimized bracket to the support. The presence of the holes can be explained from the von Mises stress envelopes, which show low stress values close to the regions where the holes are located.

Figure 12 shows the von Mises stress maps at various instances in time for each of the designs displayed in Fig. 10. The results show that the elements at the outer and inner part of the circular region as well as the slender elements connecting to the support are, in general, highly stressed during most of load duration, which suggests that the stress limit is reached at almost all time steps. To verify this hypothesis, we plot the dynamic response of the bracket as a function of time, as shown in Fig. 13. The figure displays

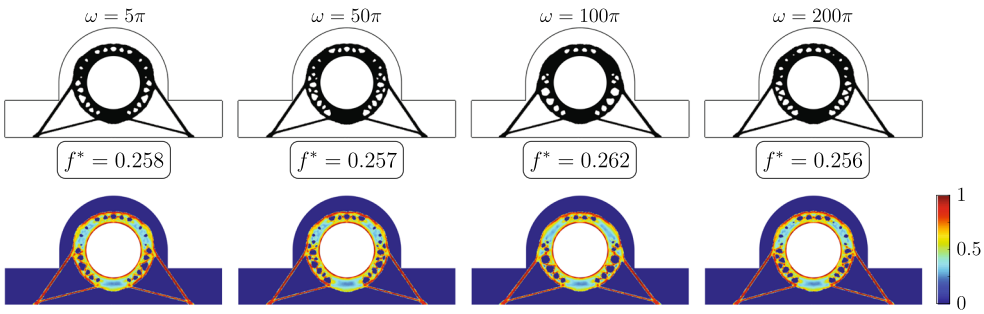

Fig. 11 Pillow bracket topologies (top) and von Mises stress envelopes (bottom) obtained for various angular frequencies: (**a**) $\omega = 5\pi$ rad/s, (**b**) $\omega = 50\pi$ rad/s, (**c**) $\omega = 100\pi$ rad/s, and (**d**) $\omega = 200\pi$ rad/s. The values of f^* correspond to the optimized volume fractions, $f(\mathbf{z}^*)$, for each design

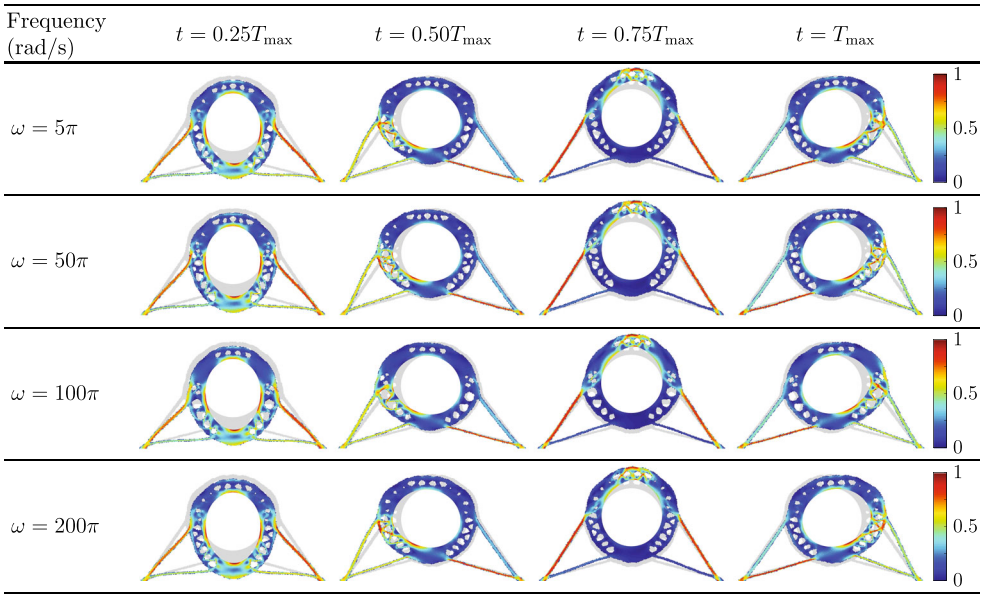

Fig. 12 Snapshots displaying the evolution of the von Mises stress maps for the designs shown in Fig. 11

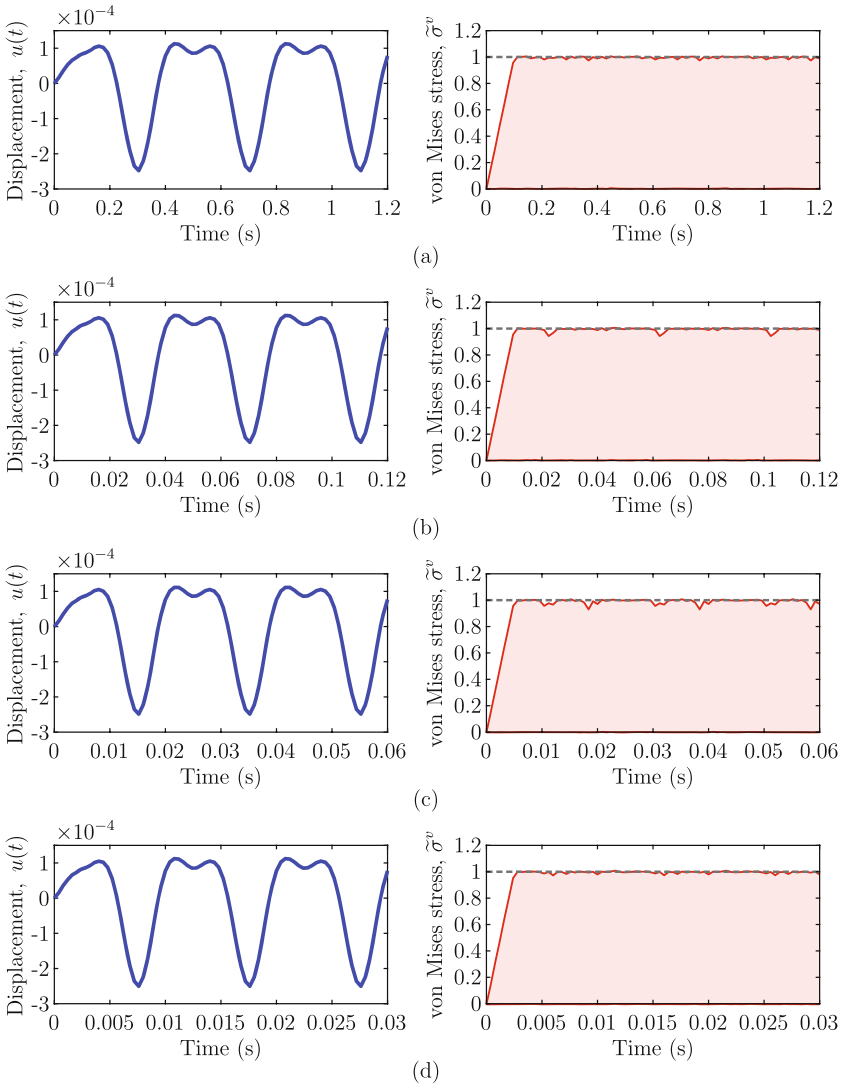

Fig. 13 Dynamic response of the pillow bracket designs of Fig. 11: (**a**) $\omega = 5\pi$ rad/s, (**b**) $\omega = 50\pi$ rad/s, (**c**) $\omega = 100\pi$ rad/s, and (**d**) $\omega = 200\pi$ rad/s. The figures on the left display the time history of vertical displacement at the lowermost point of the inner circle of the bracket and those on the right display the time history of minimum and maximum von Mises stresses for each of the optimized designs

both the vertical displacements at the lowermost node of the inner circular region of the bracket and the history of maximum and minimum von Mises stress, and as clearly seen, the stress limit for this example is reached at almost every time step.

7.4 Wheel design under rotating loads

The final example aims to design a wheel subjected to normal and shear tractions that rotate at a prescribed angular velocity, $\omega = 50\pi$ rad/s, to simulate the contact forces exerted by the ground to the wheel while it moves at a constant speed. The geometry of the wheel and the applied loads are shown in Fig. 14. The loading setup is meant to approximate the contact forces on the wheel yet, for simplicity, we neglect the inertial forces (design-dependent loads) that would act on a rotating wheel. The magnitude of the loads and additional input parameters needed to solve this example are provided in Table 5.

We obtain several optimized designs considering pattern repetition on a discretized domain meshed with 30,000 polygonal finite elements. We consider pattern repetition because it allows obtaining several optimized designs from which we can choose. We enforce the pattern repetition through the filter operator, **P**, as discussed by Talischi et al. (2012b) and by Giraldo-Londoño and Paulino (2021b). The optimized topologies and von Mises stress envelopes for different number of pattern repetitions, N_p, are shown in Fig. 15. The results show that, independently of the number of pattern repetitions, the stress constraints are satisfied at all points for the entire load duration. One peculiar

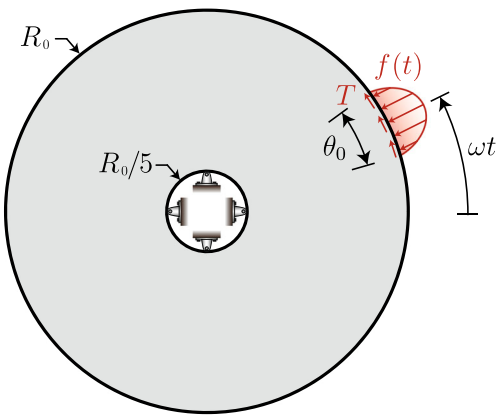

Fig. 14 Wheel domain and boundary conditions. The wheel is subjected to normal and shear tractions that are meant to represent the contact forces exerted by the ground on a wheel moving at a constant speed. The normal traction is of magnitude $f(t)$ and distributed non-uniformly according to a sine function. The shear traction is of magnitude $T = \mu f(t)$, where $\mu = 0.5$ is a friction coefficient, and it is also distributed non-uniformly according to a sine function. To prevent excessive dynamic amplification effects, we ramp both loads linearly from 0 at $t = 0$ to their full magnitude at $t = \pi/(2\omega)$

Table 5 Input parameters for the wheel

Outer radius, R_0	0.225 m
Thickness, h_0	0.02 m
Normal load, P	12×10^4 N
Shear load, T	6×10^4 N
Contact angle, θ_0	15°
Young's modulus of solid material, E_0	70 GPa
Poisson's ratio of solid material, ν_0	0.3
Mass density of solid material, ρ_0	2700 kg/m^3
Stress limit, σ_{lim}	550 MPa
Simulation time, T_{max}	0.08 s
Number of time steps, N_t	60
Rayleigh damping parameters, α_r and β_r	$[0.5,\ 1 \times 10^{-6}]$
Filter radius and filter exponent, R and q	1.2×10^{-2} m and 3

characteristic of all these designs is the highly redundant topology observed close to the rim of the wheel, which distribute the stresses around the wheel more uniformly and transmit the loads to the spokes, which then transmit the loads to the support (i.e., the axle). The redundancy observed in these designs is likely produced by the dynamic loads that change in position, thus resembling a many-load-case design scenario.

Although all designs from Fig. 15 satisfy the stress constraints locally, their dynamic performance could be different depending on the number of pattern repetitions, N_p. To verify this hypothesis, Fig. 16 displays the dynamic response (both displacements and stresses) for each of the designs as a function of time. Figures 16a–d (left) show the time history of vertical displacements at a point on the rim of the wheel at an angle of 0° measured from the horizontal line and Figs. 16a–d (right) shows the time history of maximum and minimum von Mises stress for elements with density greater than 0.5. As shown by the results, the displacements tend to become smaller as N_p increases, which indicates that the designs become stiffer for larger values of N_p. The results also show that, depending on the design, the stress limit is reached at a few peak points or at almost all points during the duration of the dynamic load. Based on these observations, we conclude that better designs can be achieved when a large number of repeated patterns are used (e.g., $N_p = 8$ for the results shown here) because the wheel tends to deform less and all stress constraints are satisfied.

8 Concluding remarks

We have introduced an AL-based formulation for topology optimization with local stress constraints of structures subjected to general dynamic loading. Given that the AL

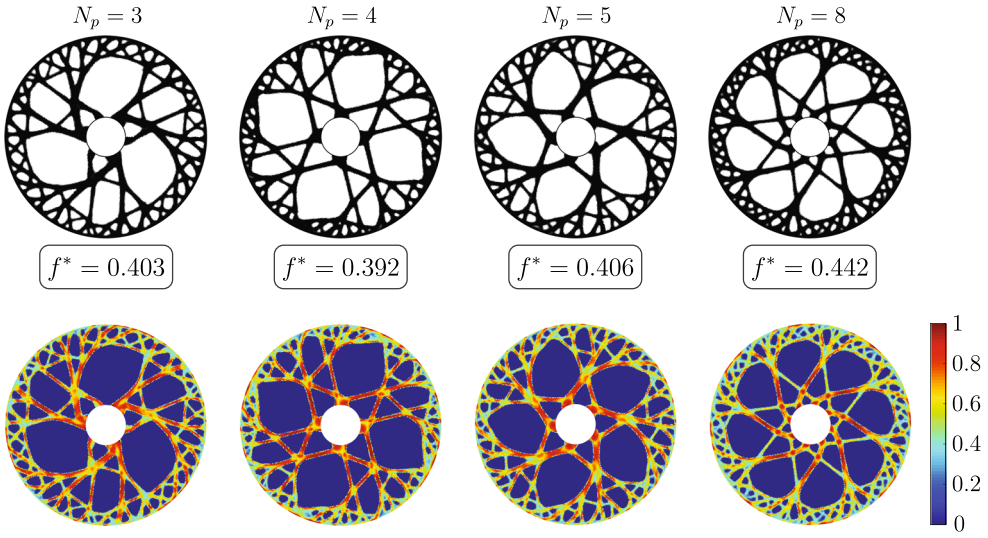

Fig. 15 Optimized topologies (top) and von Mises stress envelopes (bottom) of the wheel considering different numbers of pattern repetitions, N_p. The values of f^* correspond to the optimized volume fractions, $f(\mathbf{z}^*)$, for each design

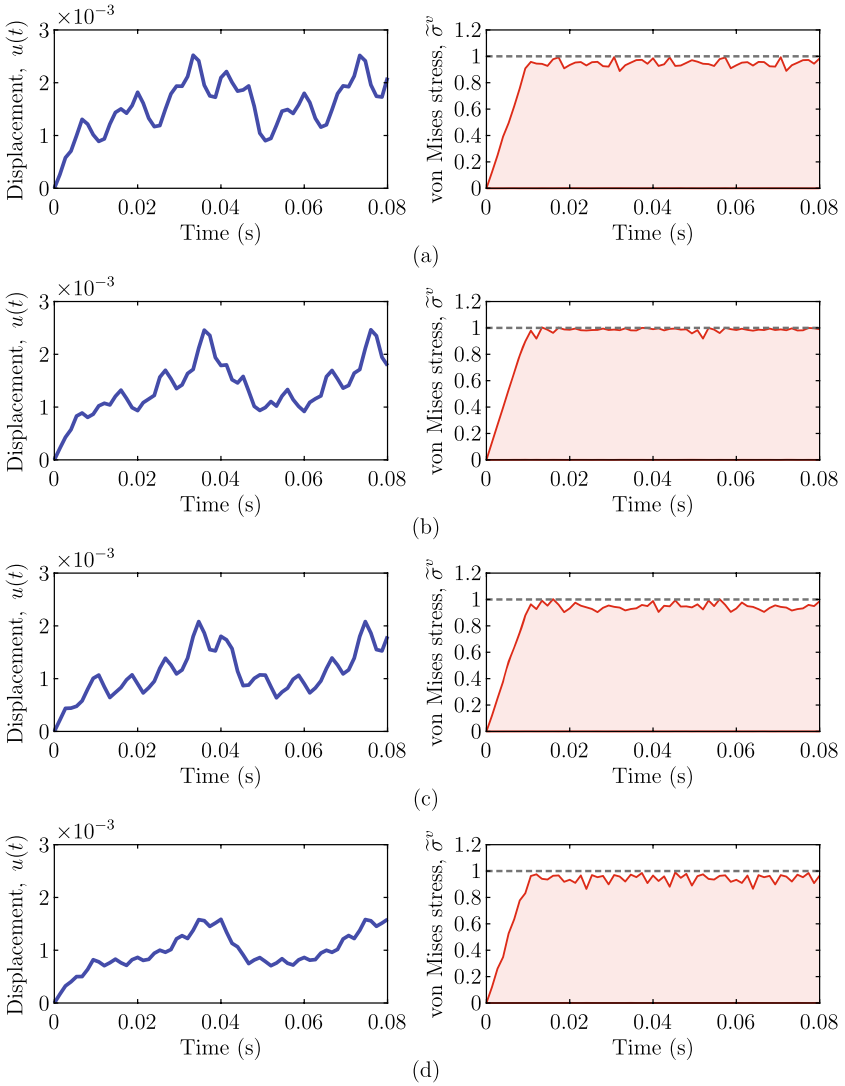

Fig. 16 Dynamic response of the wheel designs of Fig. 15: (**a**) $N_p = 3$, (**b**) $N_p = 4$, (**c**) $N_p = 5$, and (**d**) $N_p = 8$. The figures on the left display the time history of vertical displacement at outermost point of the wheel located at and angle $\theta = 0°$ from the horizontal line, and those on the right display the time history of minimum and maximum von Mises stresses for each of the optimized designs

method solves the original problem with local constraints as a sequence of optimization sub-problems, the approach adopted in this study naturally leads to designs that satisfy stress constraints locally at all time steps. We enable the method to solve problems with a large number of constraints by normalizing the penalty term of the AL function (i.e., the term containing all constraints) by the total number of constraints, NN_t, in which N is the number of elements in the FE mesh and N_t is the number of time steps of the dynamic analysis. We use this method to solve a variety of dynamic, stress-constrained problems with various mesh sizes without modifying the initial parameters of the AL function (i.e., the initial Lagrange multiplier estimators, $\lambda_{\ell i}^{(1)}$ and the initial quadratic penalty terms, $\mu_{\ell i}^{(1)}$).

To solve the AL sub-problems efficiently, we employ gradient-based algorithms and compute the sensitivities of the AL function using the *discretize-then-differentiate* adjoint variable method, in which the adjoint problem is defined based on the discretized optimization statement (both in space and time). Since the *discretize-then-differentiate* approach is tied up to a specific time integrator, we solve the dynamic analysis problem using the HHT-α method, which is a generalization of the Newmark-β method and can simplify to other classical time integration schemes given an appropriate choice of numerical parameters.

We solve several design problems to demonstrate the capabilities of the AL-based approach to solve problems with various geometries and loading conditions. As the results demonstrate, the approach employed in this study renders optimized designs that satisfy the stress constraints, within the prescribed tolerance, at every time step. To the authors' knowledge, this is the first study in the literature that satisfactorily solves stress-constrained topology optimization problems for general dynamic loading.

Appendix A: AL-tailored MMA version

We update the design variables using a version of the method of moving asymptotes (MMA) (Svanberg 1987) especially designed to solve AL optimization problems. We use this simplification because each AL sub-problem is an unconstrained optimization problem. At each AL step, k, we approximate the AL sub-problem (16) with the following minimization problem:

$$\begin{aligned} \min_{\mathbf{z}\in[0,1]^N} \quad & \tilde{J}^{(k)}(\mathbf{z}) = r^{(k)} + \sum_{\ell=1}^{N}\left(\frac{p_\ell^{(k)}}{U_\ell^{(k)} - z_\ell} + \frac{q_\ell^{(k)}}{z_\ell - L_\ell^{(k)}}\right) \\ \text{s.t:} \quad & \bar{\alpha}_\ell^{(k)} \le z_\ell \le \bar{\beta}_\ell^{(k)}, \quad \ell = 1, \ldots, N, \end{aligned} \tag{45}$$

where $L_\ell^{(k)}$ and $U_\ell^{(k)}$ are the lower and upper asymptotes, respectively, and

$$r^{(k)} = J(\mathbf{z}^{(k)}) - \sum_{\ell=1}^{N}\left(\frac{p_\ell^{(k)}}{U_\ell^{(k)} - z_\ell^{(k)}} + \frac{q_\ell^{(k)}}{z_\ell^{(k)} - L_\ell^{(k)}}\right), \tag{46}$$

$$p_\ell^{(k)} = (U_\ell^{(k)} - z_\ell^{(k)})^2\left[\max\left(\frac{\partial J}{\partial z_\ell}, 0\right) + \tau\left|\frac{\partial J}{\partial z_\ell}\right| + \frac{\theta}{U_\ell^{(k)} - L_\ell^{(k)}}\right], \tag{47}$$

and

$$q_\ell^{(k)} = (z_\ell^{(k)} - L_\ell^{(k)})^2\left[-\min\left(\frac{\partial J}{\partial z_\ell}, 0\right) + \tau\left|\frac{\partial J}{\partial z_\ell}\right| + \frac{\theta}{U_\ell^{(k)} - L_\ell^{(k)}}\right]. \tag{48}$$

Moreover, $\bar{\alpha}_\ell^{(k)} = \max[\underline{z}_\ell, \alpha_\ell^{(k)}]$ and $\bar{\beta}_\ell^{(k)} = \min[\bar{z}_\ell, \beta_\ell^{(k)}]$ are the lower and upper bounds for each MMA sub-problem, respectively, in which $\alpha_\ell^{(k)} = 0.9L_\ell^{(k)} + 0.1z_\ell^{(k)}$ and $\beta_\ell^{(k)} = 0.9U_\ell^{(k)} + 0.1z_\ell^{(k)}$, and $\underline{z}_\ell$ and $\bar{z}_\ell$ are obtained as $\underline{z}_\ell = \max[0, z^{(k)} - \texttt{move}]$ and $\bar{z}_\ell = \min[1, z^{(k)} + \texttt{move}]$, where move is a prescribed move limit (Svanberg 1987). Additional details including the definition of $L_\ell^{(k)}$, $U_\ell^{(k)}$, can be found in Giraldo-Londoño and Paulino (2021b).

The MMA sub-problem (45) can be solved analytically and its solution is given by

$$z_\ell^* = \max\{\bar{\alpha}_\ell^{(k)}, \min[\bar{\beta}_\ell^{(k)}, B_\ell]\}, \tag{49}$$

where

$$B_\ell = \frac{L_\ell^{(k)} p_\ell^{(k)} - U_\ell^{(k)} q_\ell^{(k)} + (U_\ell^{(k)} - L_\ell^{(k)})\sqrt{p_\ell^{(k)} q_\ell^{(k)}}}{p_\ell^{(k)} - q_\ell^{(k)}}. \tag{50}$$

The interested reader is referred to Giraldo-Londoño and Paulino (2021b) for the numerical implementation of the AL-tailored MMA design variable update scheme.

Appendix B: Convergence plots for selected problems

Figure 17 presents the convergence plots for both volume fraction, $f(\mathbf{z}^{(k)})$, and maximum von Mises stress, $\max(\widetilde{\boldsymbol{\sigma}}^v)$, for some of the results reported in Section 7.

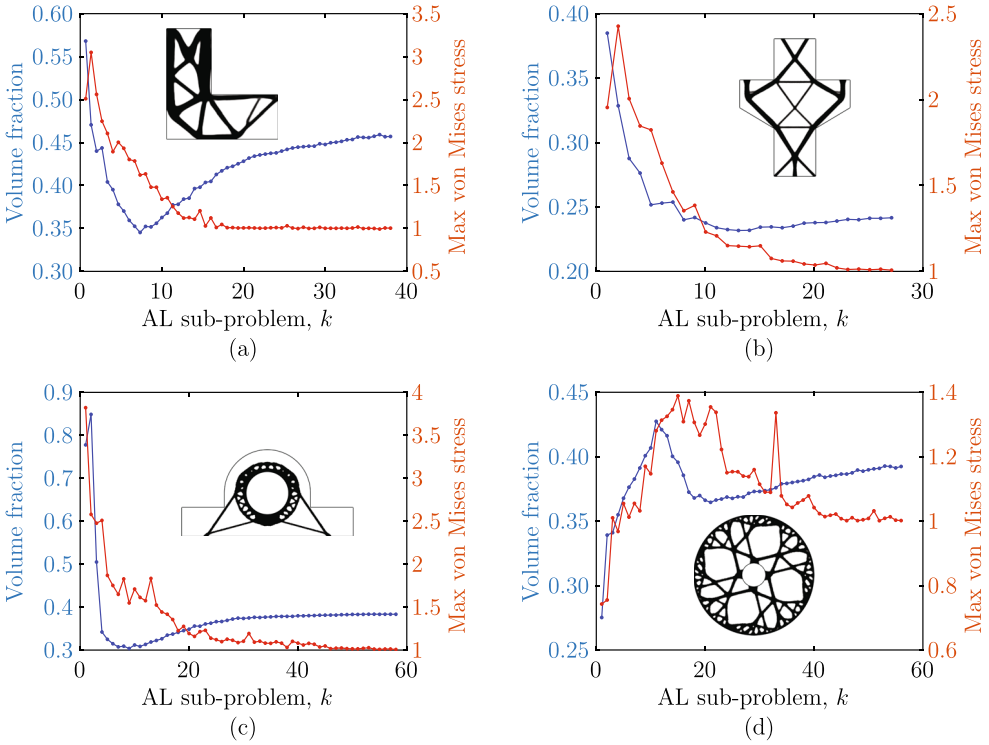

Fig. 17 Convergence plots for representative problems: (**a**) L-bracket design with $\omega = 150\pi$ rad/s, (**b**) corbel design for the case when $f_1(t)$ and $f_2(t)$ are out of phase and $\omega = 500\pi$ rad/s, (**c**) pillow bracket design with $\omega = 200\pi$ rad/s, and (d) wheel design with $N_p = 4$ pattern repetitions

Appendix C: Nomenclature

N	Number of elements in the finite element mesh
N_t	Number of time steps
$T_{\max}$	Maximum simulation time
p_0	RAMP penalization parameter
R	Filter radius
q	Nonlinear filter exponent
$J^{(k)}(\mathbf{z}, \mathbf{u}_0, \ldots, \mathbf{u}_{N_t})$	Augmented Lagrangian function at the k-th sub-problem
$f(\mathbf{z})$	Volume fraction of the structure
$g_{\ell i}(\mathbf{z}, \mathbf{u}_i)$	Stress constraint of element ℓ at time step i
$h_{\ell i}(\mathbf{z}, \mathbf{u}_i)$	Equality constraint for element ℓ at time step i used for the AL method with inequality constraints
E_0	Young's modulus of solid material
α, β, γ	Parameters used in the HHT-α method
$\tilde{\alpha}$	Parameter used to define the update of the penalty factors $\mu_{\ell i}^{(k)}$
$\alpha_{\ell i}$	Parameter used to update the penalty factor, $\mu_{\ell i}^{(k)}$, of element ℓ at time step i
$\mu_{\max}$	Maximum quadratic penalty factor
$\sigma_{\ell i}^{v}$	von Mises stress at the centroid of element ℓ at time step i
$\widetilde{\sigma}_{\ell i}^{v}$	Relaxed von Mises stress at the centroid of element ℓ at time step i
$\sigma_{\lim}$	Material stress limit in uniaxial tension
$\bar{\beta}$	Parameter used to control the aggressiveness of the threshold projection function
$\bar{\eta}$	Threshold density value used in the threshold projection function
Δt	Time increment
ϵ	Ersatz stiffness parameter
α_r and β_r	Rayleigh damping parameters
$\lambda_{\ell i}^{(k)}$	Lagrange multiplier estimator of element ℓ at time step i for the k-th AL sub-problem
$\mu_{\ell i}^{(k)}$	Quadratic penalty factor of element ℓ at time step i for the k-th AL sub-problem
ν_0	Poisson's ratio of solid material
ρ_0	Mass density of solid material
$\mathbf{V}_0$	von Mises matrix for plane stress
$\mathbf{D}_0$	Material moduli matrix of solid material
$\mathbf{B}_\ell$	Strain displacement matrix at the centroid of element ℓ
$\mathbf{z}$	Vector of design variables

$\mathbf{y} = \mathbf{P}\mathbf{z}$	Vector of filtered densities
$\mathbf{V} = \widetilde{m}_V(\mathbf{y})$	Vector of element volume fractions
$\mathbf{E} = \widetilde{m}_E(\mathbf{y})$	Vector of element stiffness parameters
$\mathbf{K}$	Global stiffness matrix
$\mathbf{k}_\ell$	Stiffness matrix of element ℓ
$\mathbf{M}$	Global mass matrix
$\mathbf{C}$	Global damping matrix
$\mathbf{m}_\ell$	Mass matrix of element ℓ
$\mathbf{u}_i$	Global displacement vector at time step i
$\mathbf{u}_{\ell i}$	Displacement vector of element ℓ at time step i
$\mathbf{f}_i$	Global load vector at time step i
$\mathbf{P}$	Filter matrix
$\mathbf{A} = \{\Omega_\ell\}_{\ell=1}^N$	Vector of element areas (2D) or element volumes (3D)
$\boldsymbol{\xi}_i$, $\boldsymbol{\mu}_i$, $\boldsymbol{\nu}_i$	Adjoint vectors at time step i used in the discretized-then-differentiate adjoint variable method

Acknowledgements We acknowledge Sandia National Laboratories, a multimission laboratory managed and operated by National Technology and Engineering Solutions of Sandia, LLC, a wholly owned subsidiary of Honeywell International, Inc., for the US Department of Energy's National Nuclear Security Administration under contract DE-NA0003525.

Compliance with ethical standards

Conflict of interest The authors declare that they have no conflict of interest.

Disclaimer The interpretation of the results of this work is solely that by the authors, and it does not necessarily reflect the views of the sponsors or sponsoring agencies.

Replication of results To facilitate replication of the results, the paper discusses the formulation in detail and provides the input parameters for each of the numerical examples.

References

Amstutz S, Novotny AA (2010) Topological optimization of structures subject to Von Mises stress constraints. Struct Multidiscip Optim 41(3):407–420

Andreani R, Haeser G, Schuverdt ML, Silva PJ (2012) A relaxed constant positive linear dependence constraint qualification and applications. Math Program 135(1-2):255–273

Arora JS, Cardoso JB (1992) Variational principle for shape design sensitivity analysis. AIAA J 30(2):538–547

Bendsøe MP, Sigmund O (2003) Topology optimization: theory, methods and applications. Springer, Berlin.

Bertsekas DP (1999) Nonlinear programming, 2nd edn. Athena Scientific, Nashua

Bruggi M (2008) On an alternative approach to stress constraints relaxation in topology optimization. Struct Multidiscip Optim 36(2):125–141

Bruggi M, Duysinx P (2012) Topology optimization for minimum weight with compliance and stress constraints. Struct Multidiscip Optim 46(3):369–384

Cheng GD, Guo X (1997) ε-relaxed approach in structural topology optimization. Struct Optim 13(4):258–266

Cheng GD, Jiang Z (1992) Study on topology optimization with stress constraints. Eng Optim 20(2):129–148

Dahl J, Jensen JS, Sigmund O (2008) Topology optimization for transient wave propagation problems in one dimension. Struct Multidiscip Optim 36(6):585–595

De Leon DM, Alexandersen J, Fonseca JS, Sigmund O (2015) Stress-constrained topology optimization for compliant mechanism design. Struct Multidiscip Optim 52(5):929–943

Elesin Y, Lazarov BS, Jensen JS, Sigmund O (2012) Design of robust and efficient photonic switches using topology optimization. Photon Nanostruct Fund Appl 10(1):153–165

Emmendoerfer Jr H, Fancello EA (2014) A level set approach for topology optimization with local stress constraints. Int J Numer Methods Eng 99(2):129–156

Emmendoerfer Jr H, Fancello EA (2016) Topology optimization with local stress constraint based on level set evolution via reaction-diffusion. Comput Methods Appl Mech Eng 305:62–88

Giraldo-Londoño O, Paulino GH (2021a) `PolyDyna`: a Matlab implementation for topology optimization of structures subjected to dynamic loads. Struct Multidiscipl Optim. 64:957–990

Giraldo-Londoño O, Paulino GH (2021b) `PolyStress`: a Matlab implementation for local stress-constrained topology optimization considering material nonlinearity. Struct Multidiscipl Optim 63:2065–2097

Giraldo-Londoño O, Paulino GH (2020) A unified approach for topology optimization with local stress constraints considering various failure criteria: von Mises, Drucker–Prager, Tresca, Mohr–Coulomb, Bresler–Pister, and William–Warnke. Proc Royal Soc A 476(2238):20190861

Guo X, Zhang WS, Wang MY, Wei P (2011) Stress-related topology optimization via level set approach. Comput Methods Appl Mech Eng 200(47-48):3439–3452

Hilber HM, Hughes TJ, Taylor RL (1977) Improved numerical dissipation for time integration algorithms in structural dynamics. Earthquake Eng Struct Dyn 5(3):283–292

Holmberg E, Torstenfelt B, Klarbring A (2013a) Global and clustered approaches for stress constrained topology optimization and deactivation of design variables. In: 10th World Congress on Structural and Multidisciplinary Optimization, Orlando, Florida, USA, pp 1–10

Holmberg E, Torstenfelt B, Klarbring A (2013b) Stress constrained topology optimization. Struct Multidiscip Optim 48(1):33–47

Izmailov AF, Solodov MV, Uskov EI (2012) Global convergence of Augmented Lagrangian methods applied to optimization problems with degenerate constraints, including problems with complementarity constraints. SIAM J Optim 22(4):1579–1606

Jensen JS, Nakshatrala PB, Tortorelli DA (2014) On the consistency of adjoint sensitivity analysis for structural optimization of linear dynamic problems. Struct Multidiscip Optim 49:831–837

Kreisselmeier G, Steinhauser R (1979) Systematic control design by optimizing a vector performance index. FAC Proc Vol 12(7):113–117. IFAC Symposium on Computer Aided Design of Control Systems, Zurich, Switzerland, 29-31 August

Le C, Bruns TE, Tortorelli DA (2012) Material microstructure optimization for linear elastodynamic energy wave management. J Mech Phys Solids 60(2):351–378

Le C, Norato J, Bruns T, Ha C, Tortorelli D (2010) Stress-based topology optimization for continua. Struct Multidiscip Optim 41(4):605–620

Lee E, James KA, Martins JRRA (2012) Stress-constrained topology optimization with design-dependent loading. Struct Multidiscip Optim 46(5):647–661

Long K, Wang X, Liu H (2019) Stress-constrained topology optimization of continuum structures subjected to harmonic force excitation using sequential quadratic programming. Struct Multidiscip Optim 59(5):1747–1759

Luo Y, Wang MY, Kang Z (2013) An enhanced aggregation method for topology optimization with local stress constraints. Comput Methods Appl Mech Eng 254:31–41

Mello LAM, Salas RA, Silva ECN (2012) On response time reduction of electrothermomechanical MEMS using topology optimization. Comput Methods Appl Mech Eng 247:93–102

Min S, Kikuchi N, Park YC, Kim S, Chang S (1999) Optimal topology design of structures under dynamic loads. Struct Optim 17(2-3):208–218

Nakshatrala PB, Tortorelli DA (2016) Nonlinear structural design using multiscale topology optimization. Part II: transient formulation. Comput Methods Appl Mech Eng 304:605–618

Newmark NM (1959) A method of computation for structural dynamics. J Eng Mech Div 85(3):67–94

Nocedal J, Wright SJ (2006) Numerical optimization, 2nd edn. Springer, New York

Nomura T, Sato K, Taguchi K, Kashiwa T, Nishiwaki S (2007) Structural topology optimization for the design of broadband dielectric resonator antennas using the finite difference time domain technique. Int J Numer Methods Eng 71(11):1261–1296

Paris J, Navarrina F, Colominas I, Casteleiro M (2009) Topology optimization of continuum structures with local and global stress constraints. Struct Multidiscip Optim 39(4):419–437

Paris J, Navarrina F, Colominas I, Casteleiro M (2010) Block aggregation of stress constraints in topology optimization of structures. Adv Eng Softw 41(3):433–441

Park YK (1995) Extensions of optimal layout design using the homogenization method. Ph.D thesis, University of Michigan, Ann Arbor

Pereira JT, Fancello EA, Barcellos CS (2004) Topology optimization of continuum structures with material failure constraints. Struct Multidiscip Optim 26(1-2):50–66

Senhora FV, Giraldo-Londoño O, Menezes IFM, Paulino GH (2020) Topology optimization with local stress constraints: a stress aggregation-free approach. Struct Multidiscip Optim 62:1639–1668

Stolpe M, Svanberg K (2001) On the trajectories of the epsilon-relaxation approach for stress-constrained truss topology optimization. Struct Multidiscip Optim 21(2):140–151

Svanberg K (1987) The method of moving asymptotes—a new method for structural optimization. Int J Numer Methods Eng 24(2):359–373

Talischi C, Paulino GH, Pereira A, Menezes IFM (2012a) Polymesher: a general-purpose mesh generator for polygonal elements written in Matlab. Struct Multidiscip Optim 45(3):309–328

Talischi C, Paulino GH, Pereira A, Menezes IFM (2012b) Polytop: a Matlab implementation of a general topology optimization framework using unstructured polygonal finite element meshes. Struct Multidiscip Optim 45(3):329–357

Turteltaub S (2005) Optimal non-homogeneous composites for dynamic loading. Struct Multidiscip Optim 30(2):101–112

von Mises R (1913) Mechanik der festen koerper in plastisch deformahlem zustand. Goettinger Narchrichten 4:582–592

Wang F, Lazarov BS, Sigmund O (2011) On projection methods, convergence and robust formulations in topology optimization. Struct Multidiscip Optim 43(6):767–784

Xia L, Zhang L, Xia Q, Shi T (2018) Stress-based topology optimization using bi-directional evolutionary structural optimization method. Comput Methods Appl Mech Eng 333:356–370

Yoon GH (2010) Structural topology optimization for frequency response problem using model reduction schemes. Comput Methods Appl Mech Eng 199(25-28):1744–1763

Zegard T, Paulino GH (2016) Bridging topology optimization and additive manufacturing. Struct Multidiscip Optim 53(1):175–192

Zhang X, Kang Z (2014) Dynamic topology optimization of piezoelectric structures with active control for reducing transient response. Comput Methods Appl Mech Eng 281:200–219

Zhao J, Wang C (2016) Dynamic response topology optimization in the time domain using model reduction method. Struct Multidiscip Optim 53(1):101–114

Zhao J, Wang C (2017) Topology optimization for minimizing the maximum dynamic response in the time domain using aggregation functional method. Comput Struct 190:41–60